

Chapter 6: Poroelasticity and tidal loading

6.1 Introduction

It is established above, in Chapter 4, that there are many known examples of the tidal modulation of seafloor hydrothermal systems. Variations in temperature, effluent velocity and chemistry can often be correlated to the local ocean tide, and it is therefore expected that the changing tidal pressure field on the seafloor is responsible for a majority of the observed tidal signals. In contrast, Chapter 5 is concerned with the *steady-state* structure of a seafloor convection cell, and in particular its dependence on the properties of water. The aim of this chapter is to establish whether the nonlinear thermodynamic properties of water (Chapter 5) are sufficient to explain the tidal signals which have been observed at mid-ocean ridge hydrothermal systems (Chapter 4).

The effect of tidal loading on subseafloor convection cells is investigated with reference to the equations of poroelasticity, which describe the response of a fluid-filled porous medium to applied stress (Biot, 1941; Rice & Cleary, 1976; Van der Kamp & Gale, 1983; Kämpel, 1991). When a porous medium is placed under load, the resultant stress is borne partly by the solid matrix and partly by the interstitial fluid where it is manifest as a change in fluid pressure known as the incremental pore pressure. The partitioning of the total stress between the fluid and the solid matrix is a function of their elastic properties and the porosity. Consequently, if any one of these properties varies spatially, it is possible for a locally *uniform* load, such as the ocean tide, to produce a *non-uniform* incremental pore pressure field. The subsequent spatial gradients in the incremental pore pressure can then drive interstitial fluid from one region of the fluid-filled medium to another.

For this reason, it is of great interest to consider how the poroelastic properties of a subseafloor convection cell vary spatially. As in Chapter 5, it is assumed for simplicity that the elastic and transport properties of the solid matrix are constant and homogeneous. The only source of spatial variability is the interstitial fluid, whose properties are known to be strongly dependent on temperature. For example, it is shown that the bulk modulus of water changes significantly over the temperature range encountered in a subseafloor hydrothermal system. The partitioning of the total tidal stress between the matrix and the interstitial fluid

differs markedly between regions where the fluid is liquid-like and regions where it is gas-like. When tidal loading is applied at the seafloor, the gradients in incremental pore pressure induce tidally modulated fluid flow between the cold, liquid-like regions and the hot, gas-like regions.

The physical quantities associated with the fluid in a subseafloor convection cell - such as pressure, velocity and temperature (Section 5.3) – are expected to fluctuate as a result of tidal loading. The label ‘incremental’ is used to refer to the tidally induced variation of any physical quantity about its undisturbed value. For some years, there has been a well-established analytical solution giving the incremental pore pressure in an infinite one-dimensional halfspace subject to uniform tidal loading (Van der Kamp & Gale, 1983; Wang & Davis, 1996). Here, this solution is extended to cover the two physical quantities which are commonly measured on the seafloor – the vertical velocity and the temperature (Chapter 4). For an infinite halfspace, it is shown that the incremental vertical velocity at the seafloor lags the ocean tide by 135° . Consequently, the maximum effluent velocity at the seafloor is predicted to occur ~ 4.5 h after high tide for semi-diurnal components, and ~ 9 h after high tide for diurnal components. If the permeable crust is taken to be of finite thickness the corresponding phase lag is shown to lie between 90° and $\sim 135^\circ$, depending on the thickness of the permeable layer relative to the lengthscale associated with pore pressure diffusion. Consequently, observed phase lags between the ocean tide and effluent velocity at the seafloor could be used to infer the vertical distance over which the crust is permeable.

An approximate expression for the tidally induced incremental temperature is derived for the case of buoyant fluid ascending through a linear temperature gradient. It is shown that the incremental temperature lags the incremental velocity by 90° . Hence, for an infinite halfspace, the incremental temperature at the seafloor lags the ocean tide by 225° and the hottest effluent is expelled ~ 7.5 h after high tide for semi-diurnal components, and ~ 15 h after high tide for diurnal components. If the permeable crust has finite thickness, however, the seafloor effluent temperature lags the ocean tide by an angle between 180° and $\sim 225^\circ$, depending on the thickness of the permeable layer. These predicted phase lags are shown to be consistent with many of the seafloor data discussed in Chapter 4.

Analytical solutions of simple one-dimensional models allow the physical processes responsible for seafloor tidal signals to be identified. In Section 6.3.2, some preliminary

numerical simulations are presented in which the two-dimensional convection cell of Section 5.3 is subjected to uniform tidal loading at the seafloor. The results of these simulations are interpreted with reference to the one-dimensional analytical solutions (Section 6.3.1).

6.2 Fundamental concepts of poroelasticity

The purpose of this section is to review the theory of poroelasticity, with particular regard to hydrothermal systems under tidal loading (Biot, 1941; Rice & Cleary, 1976; Van der Kamp & Gale, 1983; Kämpel, 1991). It is assumed that the properties of the crust are constant and homogeneous. Consequently, the objective is to investigate the effect which temperature-dependent fluid properties have on the principal poroelastic parameters.

6.2.1 The dependence of poroelastic parameters on fluid temperature

When a fluid-filled porous medium such as the ocean crust is placed under external load, it experiences incremental stress ($\hat{\sigma}_{ij}$) and incremental strain ($\hat{\epsilon}_{ij}$). Prior to loading, the absolute pressure of the fluid in the pores (p) is constant. Under load, however, there is an additional, time-varying pressure known as the incremental pore pressure (\hat{p}). The confining pressure (\hat{p}_c) is a scalar measure of the stress, defined by:

$$\hat{p}_c = -\frac{1}{3}\hat{\sigma}_{kk} \quad (6.1)$$

(The Einstein summation convention is used throughout, so that there is an implied summation over a repeated tensor suffix.) Three distinct bulk moduli are relevant to the behaviour of the fluid-filled porous medium and their physical interpretation is summarised in Figure 6.1. Firstly, the grain bulk modulus (K_g) is the bulk modulus of the medium in the absence of any pore space. Secondly, the matrix bulk modulus (K_m) is the bulk modulus of the medium when the pore space exists but is empty. (For this reason, it is sometimes known as the drained bulk modulus.) Values of the grain and matrix bulk moduli for several geological materials are reproduced in Table 6.1.

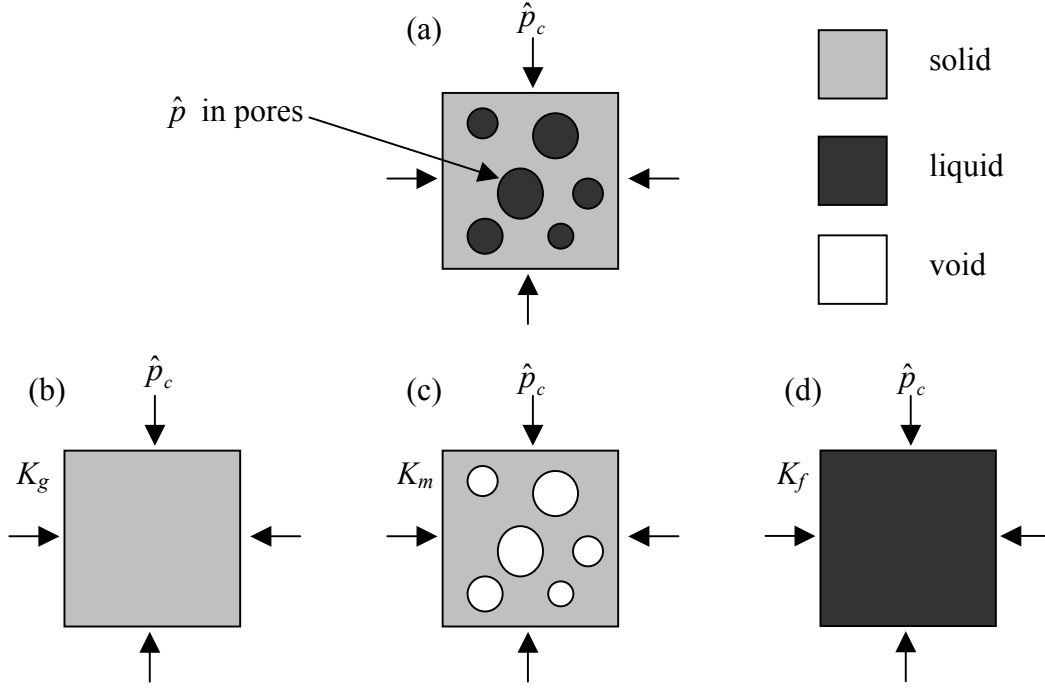


Figure 6.1: Schematic illustrations of the three bulk moduli relevant to poroelasticity. (a) A fluid-filled poroelastic medium subjected to an incremental confining pressure \hat{p}_c has incremental pore pressure \hat{p} . (b) Situation defining the grain bulk modulus: $\hat{e}_{kk} = -\hat{p}_c / K_g$. (c) Situation defining the matrix bulk modulus: $\hat{e}_{kk} = -\hat{p}_c / K_m$. (d) Situation defining the fluid bulk modulus: $\hat{e}_{kk} = -\hat{p}_c / K_f$

Thirdly, the fluid bulk modulus (K_f) is the bulk modulus of the fluid which fills the pore space, and is a function of its pressure and temperature. If the pore fluid has temperature T , specific enthalpy h , and density ρ , then the *isenthalpic* fluid bulk modulus (K_{fh}) is defined (Van Wylen & Sonntag, 1978) by:

$$K_{fh} = \left[\left(\frac{1}{\rho} \frac{\partial \rho}{\partial p} \Big|_{h=const.} \right) \right]^{-1} \quad (6.2)$$

while the *isothermal* fluid bulk modulus (K_{fT}) is defined by:

$$K_{fT} = \left[\left(\frac{1}{\rho} \frac{\partial \rho}{\partial p} \Big|_{T=const.} \right) \right]^{-1} \quad (6.3)$$

For water, the values of K_{fh} and K_{fT} are sufficiently similar to be regarded as interchangeable, and both may be considered synonymous with the fluid bulk modulus (K_f). (The values quoted in this dissertation are derived from the steam tables embedded in the

HYDROTHERM code and are, strictly, isenthalpic fluid bulk moduli.) Values of K_f are plotted in Figure 6.2 for a range of pressures and temperatures relevant to seafloor hydrothermal systems.

material	K_g (GPa)	K_m (GPa)	ν	φ_0	k (m ²)
seafloor sediment ¹	50	0.5	0.10	0.50	$1 \cdot 10^{-17}$ to $1 \cdot 10^{-15}$
seafloor sediment ²				0.60	$1 \cdot 10^{-15}$
seafloor sediment ³		2.17		0.80	$5 \cdot 10^{-15}$
Ruhr sandstone ⁴	36	13	0.12	0.02	$2 \cdot 10^{-16}$
Berea Sandstone ⁴	36	8	0.20	0.19	$2 \cdot 10^{-13}$
Weber sandstone ⁴	36	13	0.15	0.06	$1 \cdot 10^{-15}$
Charcoal granite ⁴	45	34	0.27	0.02	$1 \cdot 10^{-19}$
Westerly granite ⁴	45	25	0.25	0.01	$4 \cdot 10^{-19}$
Tennessee marble ⁴	50	40	0.25	0.02	$1 \cdot 10^{-19}$
MOR basement ⁵					$9 \cdot 10^{-12}$
“typical” Basalt ⁶		30	0.20		

Table 6.1: The transport and elastic properties of various geological materials. K_g – grain bulk modulus. K_m – matrix bulk modulus. ν – Poisson’s ratio. φ_0 – porosity. k – permeability. References: (1) Wang & Davis (1996). (2) Fang *et al.* (1993). (3) Hurley & Schultheiss (1991). (4) Van der Kamp & Gale (1983). (5) Fisher *et al.* (1997) – MOR refers to ‘Mid-Ocean Ridge’. (6) Carmichael (1982), where values for several basalts are given - typical values are reproduced here.

Figure 6.2 shows that K_f depends strongly on temperature but only weakly on pressure in the region of p - T space relevant to seafloor hydrothermal systems. The temperature dependence is similar to that of the thermodynamic properties considered in Chapter 5 (Figure 5.6), in the sense that there is a sharp change in behaviour at $\sim 400^\circ\text{C}$ as water moves from a liquid-like state to a gas-like state. At seafloor pressures, the bulk modulus of water ranges from a cold, liquid-like value of ~ 2.2 GPa at 2°C to hot, gas-like values between ~ 0.02 GPa and ~ 0.05 GPa above $\sim 400^\circ\text{C}$. (A fluid obeying the laws for a perfect gas has a bulk modulus (K_f) equal to the fluid pressure (p). At seafloor pressures, water above $\sim 400^\circ\text{C}$ approximates this perfect gas behaviour fairly closely.) Comparison of Figure 6.2a with Table 6.1 shows that the bulk modulus of water in the seafloor crust (K_f) is much smaller than the grain bulk modulus (K_g) for all of the listed geological materials. It is therefore assumed that $K_f \ll K_g$ for all subseafloor convection cells. However, it is not always true that $K_f \ll K_m$. For example,

Table 6.1 shows that K_f (~ 2.2 GPa when cold) may even exceed K_m (~ 0.5 GPa), when the poroelastic medium is sediment.

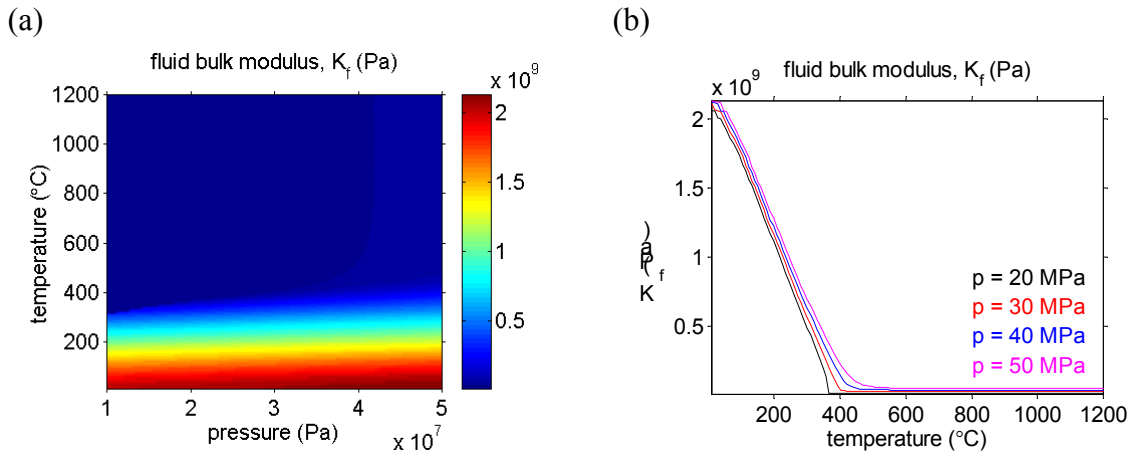


Figure 6.2: The bulk modulus of pure water, K_f . (a) K_f as a function of pressure and temperature. (b) K_f as a function of temperature at a range of typical subseafloor pressures. Data are derived from the steam tables embedded in the HYDROTHERM code. (10^7 Pa corresponds to 1 km below sea level.)

The three bulk moduli (K_g , K_m , and K_f), and the porosity (ϕ_0) together constitute a set of four fundamental parameters describing the elastic properties of a fluid-filled porous medium. Three further parameters (α , S and β) are often derived from this fundamental set, and their dependence on the thermodynamic state of the pore fluid is considered below.

6.2.1.1 Coefficient of effective stress: α

Firstly, the coefficient of effective stress (α) is defined (Nur & Byerlee, 1971) by:

$$\alpha = 1 - \frac{K_m}{K_g} \quad (6.4)$$

Hence, α is a measure of the relative magnitude of the matrix and grain bulk moduli (Table 6.1). It should be noted that $K_m \leq K_g$, and so α is a dimensionless number in the range $[0,1]$. The value of α depends solely on the properties of the rock matrix, and *not* on the properties of the interstitial fluid. Consequently, it is assumed for simplicity that α is constant and homogeneous within any particular subseafloor convection cell. For the geological materials listed in Table 6.1, the values of α range from 0.2 (Tennessee marble) to 0.99 (seafloor sediment).

6.2.1.2 Storage compressibility: S

The second derived parameter is the storage compressibility (S) defined by:

$$S = \left(\frac{1}{K_m} - \frac{1}{K_g} \right) + \phi_0 \left(\frac{1}{K_f} - \frac{1}{K_g} \right) \quad (6.5)$$

As its name implies, the storage compressibility has units of inverse pressure, and it can be interpreted as the volume of interstitial fluid which is added to the pore space, per unit volume of rock, per unit increase in pore pressure (Kümpel, 1991). Since K_g , K_m , and ϕ_0 are regarded as constants for any particular problem, it follows that spatial variations in S can only be due to spatial variations in K_f . Figure 6.2 shows that K_f changes little with pressure and is a *decreasing* function of temperature. It therefore follows from equation (6.5) that S changes little with pressure and is an *increasing* function of temperature. Table 6.1 suggests that $K_g = 50$ GPa and $K_m = 30$ GPa might be reasonable values for the bulk moduli of the oceanic crust. Unless otherwise stated, these values will be used throughout this chapter.

The fact that S depends on the fluid bulk modulus suggests that there will be a marked change in its value at $\sim 400^\circ\text{C}$, when water changes from a liquid-like state to a gas-like state. Equation (6.5) shows that the relative magnitude of this change is controlled by the value of the porosity, ϕ_0 . Consequently, a critical porosity, $\phi_c(p, T)$, can be defined by:

$$\phi_c(p, T) = \frac{\left(\frac{1}{K_m} - \frac{1}{K_g} \right)}{\left(\frac{1}{K_f} - \frac{1}{K_g} \right)} \quad (6.6)$$

It should be noted that this critical porosity depends on the fluid bulk modulus (K_f) and is therefore pressure- and temperature-dependent. The variability of S as a function of fluid temperature can now be classified into one of three regimes corresponding to large, intermediate and small values of the porosity ratio (ϕ_0 / ϕ_c). In the intermediate porosity regime - when $(\phi_0 / \phi_c) \sim 1$ for all temperatures - the full defining equation for S must be used (equation (6.5)). However, simplifications can be made when the porosity is either large or small in relation to the critical porosity, ϕ_c . For $K_g = 50$ GPa and $K_m = 30$ GPa the critical porosity (ϕ_c) is 0.03 for cold water ($K_f = 2.2$ GPa) and 0.0003 for hot water ($K_f = 0.02$ GPa). The dependence of S on pressure and temperature for the three porosity regimes is illustrated in Figure 6.3.

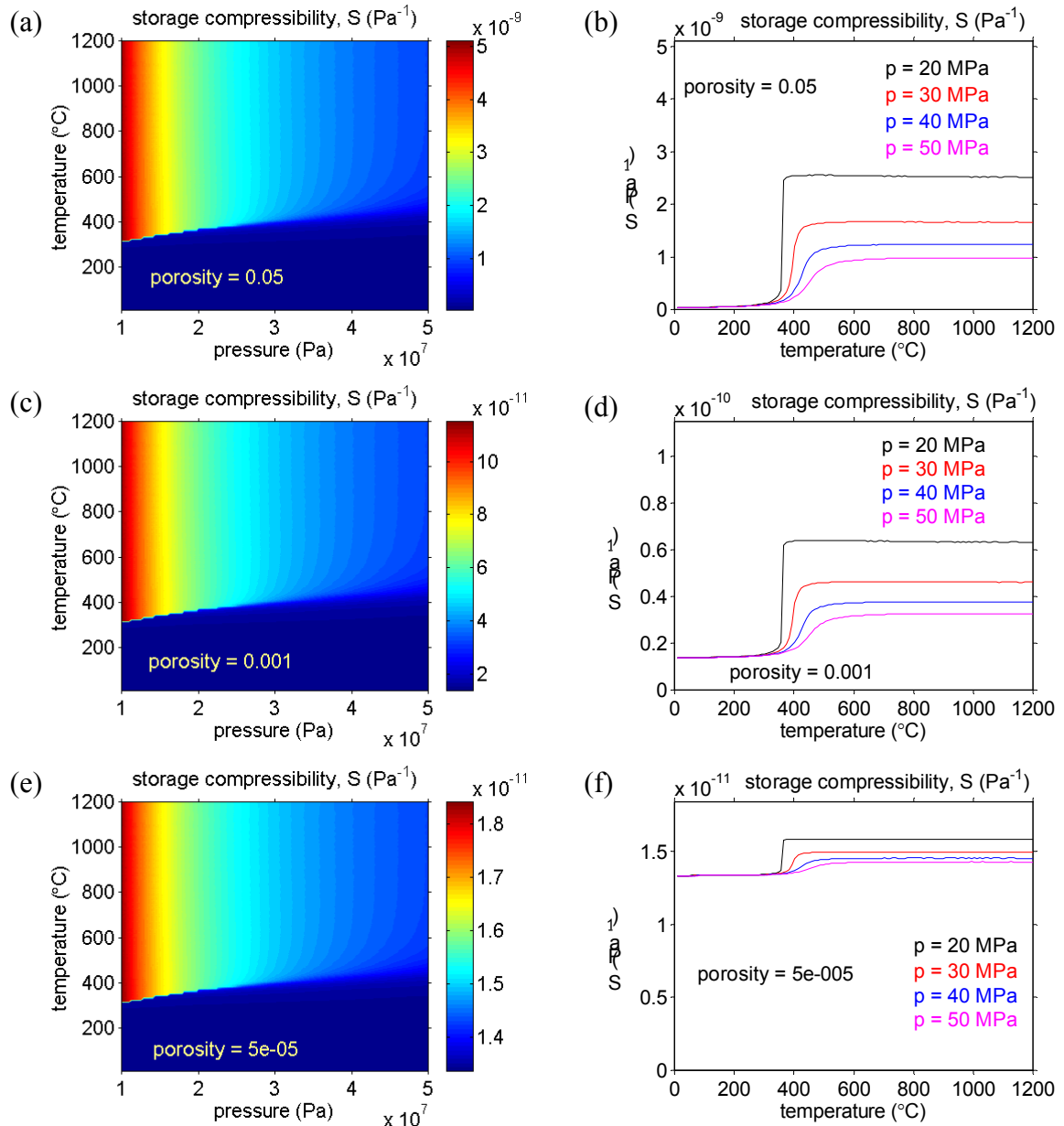


Figure 6.3: The dependence of the storage compressibility (S) on the thermodynamic state of the interstitial fluid in the large, intermediate and small porosity regimes with $K_g = 50$ GPa, $K_m = 30$ GPa. The interstitial fluid is assumed to be pure water. Thermodynamic data are taken from the tables embedded in the HYDROTHERM code. (a),(b) $\phi_0 = 0.05$ (large). (c),(d) $\phi_0 = 0.001$ (intermediate). (e),(f) $\phi_0 = 0.00005$ (small). (10^7 Pa corresponds to 1 km below sea level.)

The large porosity regime - when $(\phi_0 / \phi_c) > 1$ for all temperatures - implies that:

$$S \approx \frac{\phi_0}{K_f} \quad (6.7)$$

Equation (6.7) shows that the storage compressibility (S) is proportional to the fluid compressibility (K_f^{-1}) in the large porosity regime (Figures 6.3a,b).

In contrast, the small porosity regime - when $(\phi_0 / \phi_c) < 1$ for all temperatures - implies that

$$S \approx \left(\frac{1}{K_m} - \frac{1}{K_g} \right) = \frac{\alpha}{K_m} \quad (6.8)$$

Hence, the storage compressibility is approximately constant as a function of temperature when the porosity is small (Figures 6.3e,f).

In summary, it should be noted that S is always an *increasing* function of fluid temperature at seafloor pressures. The greatest change in S occurs at $\sim 400^\circ\text{C}$, as the water changes from a liquid-like state to a gas-like state. The contrast between the liquid-like and gas-like values of S is greatest when the porosity is large.

6.2.1.3 Skempton ratio: β

Thirdly amongst the derived poroelastic parameters, the Skempton ratio (β) is defined by

$$\beta = \frac{\left(\frac{1}{K_m} - \frac{1}{K_g} \right)}{\left(\frac{1}{K_m} - \frac{1}{K_g} \right) + \phi_0 \left(\frac{1}{K_f} - \frac{1}{K_g} \right)} \quad (6.9)$$

The Skempton ratio is a dimensionless parameter taking values in the range $[0,1]$. When a poroelastic medium is loaded isotropically, the Skempton ratio (β) can be interpreted as the ratio of the incremental pore pressure (\hat{p}) to the applied incremental confining pressure (\hat{p}_c) (Figure 6.1a). Equivalently, β is the proportion of the total applied stress which is borne by the pore fluid. Equations (6.4), (6.5) and (6.9) imply that $\beta = (\alpha / K_m) / S$. Since α and K_m are constant properties of the rock matrix, it follows that the variation of β with the thermodynamic state of the fluid can be divided into the same three porosity regimes as the variation of S .

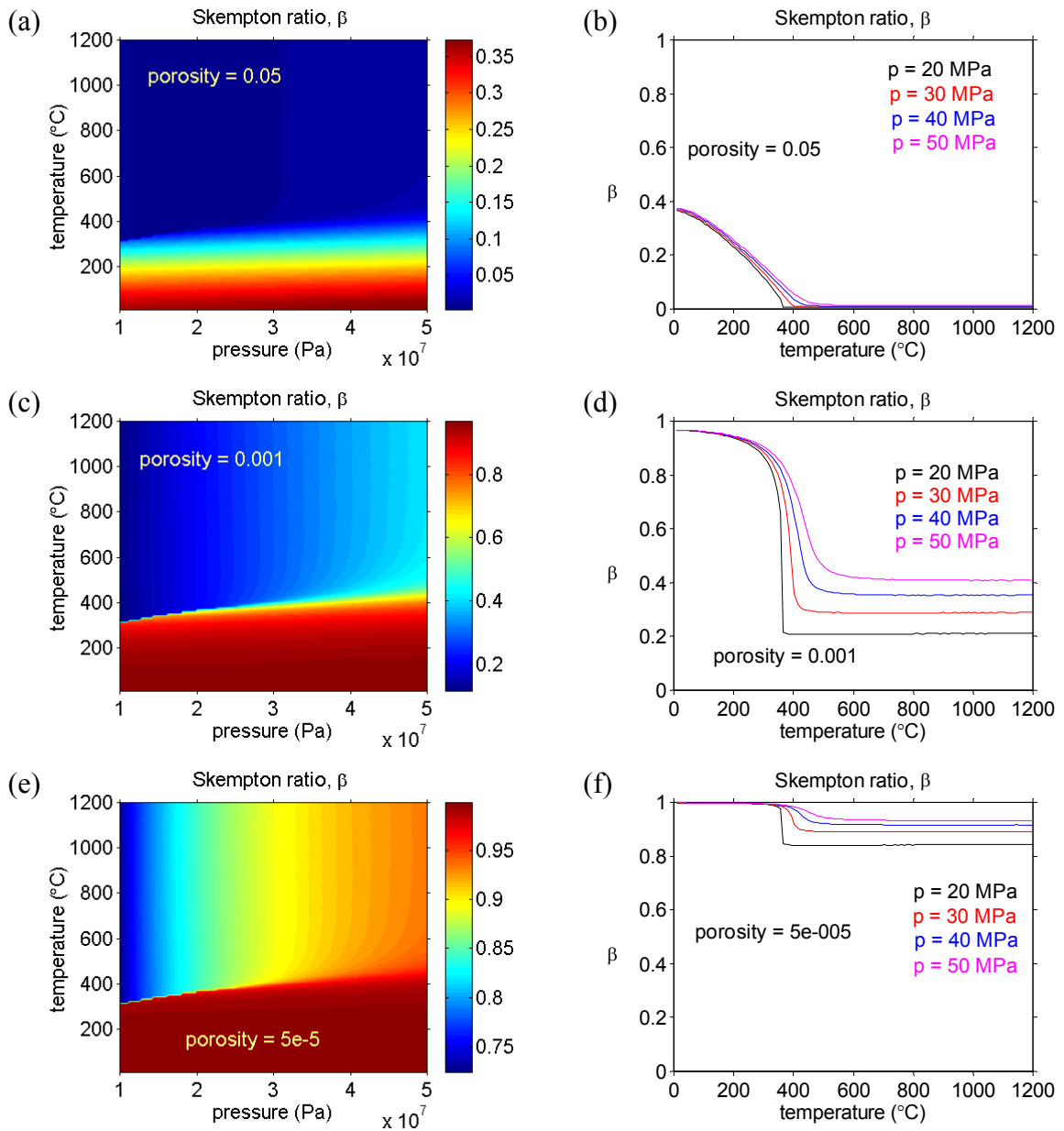


Figure 6.4: The dependence of the Skempton ratio (β) on the thermodynamic state of the interstitial fluid in the large, intermediate and small porosity regimes with $K_g = 50$ GPa, $K_m = 30$ GPa. Interstitial fluid is pure water. Thermodynamic data from the tables embedded in the HYDROTHERM code. (a), (b) $\varphi_0 = 0.05$ (large). (c), (d) $\varphi_0 = 0.001$ (intermediate). (e), (f) $\varphi_0 = 0.00005$ (small). (10^7 Pa corresponds to 1 km below sea level.)

For intermediate porosity - when $(\varphi_0 / \varphi_c) \sim 1$ - the full defining equation for β (equation (6.9)) must be used. However, for large porosity - when $(\varphi_0 / \varphi_c) > 1$ - equation (6.9) reduces to:

$$\beta \approx \left[\frac{\alpha}{\phi_0 K_m} \right] K_f \quad (6.10)$$

Hence the Skempton ratio (β) is a scaled version of the fluid bulk modulus (K_f) when the porosity is large and it is therefore highly temperature dependent (Figures 6.2a,b, 6.4a,b).

In contrast, for small porosity - when $(\phi_0 / \phi_c) < 1$ - the temperature dependence of the Skempton ratio is much reduced (Figures 6.4e,f) and equation (6.9) reduces to

$$\beta \approx 1 \quad (6.11)$$

In summary, β is a *decreasing* function of fluid temperature for all seafloor pressures, with the greatest change occurring at $\sim 400^\circ\text{C}$, where water changes from a liquid-like state to a gas-like state. The contrast between the liquid-like and gas-like values of β is greatest when the porosity is large. Since β represents the proportion of the applied stress borne by the interstitial fluid, it follows that uniform tidal loading at the seafloor can create incremental pore pressures which differ between the hot and cold parts of a hydrothermal convection cell. In general terms, when the ocean tide is high, cold regions of the cell (where β is large) will have greater pore pressures than hot regions (where β is small). Consequently, fluid is expected to flow from cold regions to hot regions at high tide. The pressure difference which drives the flow is particularly large if the hot fluid is gas-like ($> \sim 400^\circ\text{C}$) and the cold fluid is liquid-like ($< \sim 400^\circ\text{C}$). The magnitude of the induced flow is determined by the spatial gradient of the incremental pore pressure. Consequently, the induced tidally modulated flow is expected to be large where spatial gradients in temperature are large. This heuristic argument is investigated with greater rigour in Section 6.3.

6.2.2 The governing equations of poroelasticity

Given a value for the Poisson's ratio of the solid matrix (ν) it can be shown (Rice & Cleary, 1976; Van der Kamp & Gale, 1983) that the stress-strain relationship for a fluid-filled porous medium is:

$$\hat{e}_{ij} = \frac{1}{3K_m} \left[\frac{(1+\nu)}{(1-2\nu)} \hat{\sigma}_{ij} - \frac{\nu}{(1-2\nu)} \hat{\sigma}_{kk} \delta_{ij} + \alpha \hat{p} \delta_{ij} \right] \quad (6.12)$$

Typically, the Poisson's ratio takes a value $\nu \approx 0.2$ for geological materials (Table 6.1), and so $\nu = 0.2$ is assumed throughout this chapter. With the convention that a repeated suffix indicates summation, equation (6.12) yields:

$$\hat{e}_{kk} = \frac{1}{3K_m} [\hat{\sigma}_{kk} + 3\alpha \hat{p}] = -\frac{1}{K_m} [\hat{p}_c - \alpha \hat{p}] \quad (6.13)$$

Equation (6.13) can be used to provide a physical interpretation for the effective stress ratio (α). For a solid medium, the volume dilatation (\hat{e}_{kk}) is proportional to the confining pressure (\hat{p}_c) (Figure 6.1b). For a poroelastic medium, however, equation (6.13) shows that the volume dilatation is proportional to the so-called effective pressure ($\hat{p}_c - \alpha\hat{p}$).

This dissertation is concerned with the effect of tidal loading at periods of ~ 12 h and greater. This timescale is much greater than the time taken for seismic waves (speed > 1 km.s⁻¹), to cover the lengthscales appropriate to hydrothermal systems (< 10 km). Consequently, the stresses due to tidal loading of the seafloor are, effectively, transmitted instantaneously throughout a subseafloor convection cell. The equations of compatibility for an elastic medium (Love, 1927) can be applied to equation (6.12) to give an equation expressing elastic equilibrium:

$$\nabla^2 \left[(1 + \nu)\hat{\sigma}_{ij} - \nu\hat{\sigma}_{kk}\delta_{ij} \right] + \frac{\partial^2}{\partial x_i \partial x_j} \hat{\sigma}_{kk} + \alpha(1 - 2\nu) \left[\nabla^2 \hat{p}\delta_{ij} + \frac{\partial^2}{\partial x_i \partial x_j} \hat{p} \right] = 0 \quad (6.14)$$

Equation (6.14) can be contracted on the suffices to yield:

$$\nabla^2 \hat{\sigma}_{kk} + \left[\frac{2\alpha(1 - 2\nu)}{(1 - \nu)} \right] \nabla^2 \hat{p} = 0 \quad (6.15)$$

The conservation of pore fluid is expressed by the equation:

$$\left[\frac{k}{\mu S} \right] \nabla^2 \hat{p} = \frac{\partial \hat{p}}{\partial t} + \frac{\partial}{\partial t} \left(\beta \cdot \frac{\hat{\sigma}_{kk}}{3} \right) \quad (6.16)$$

where k is the permeability of the rock matrix and μ is the dynamic viscosity of the interstitial fluid.

In general, solutions to problems of poroelastic loading are found by solving equations (6.14) and (6.16) for the incremental pore pressure (\hat{p}) and the incremental stress tensor ($\hat{\sigma}_{ij}$). In certain simple cases, however, the number of unknowns reduces to two - \hat{p} and $\hat{\sigma}_{kk}$ - and solutions are found by solving equations (6.15) and (6.16). Furthermore, if $\hat{\sigma}_{kk}$ is known, equation (6.16) becomes a forced conduction equation for the incremental pore pressure (\hat{p}) with a diffusivity (κ) defined by

$$\kappa = \frac{k}{\mu S} \quad (6.17)$$

The permeability of the seafloor (k) is very poorly constrained (Table 6.1). Consequently, it is helpful to define a scaled diffusivity ($(\mu S)^{-1}$) in order to examine the dependence of the diffusivity (κ) on the temperature (T) of the interstitial fluid.

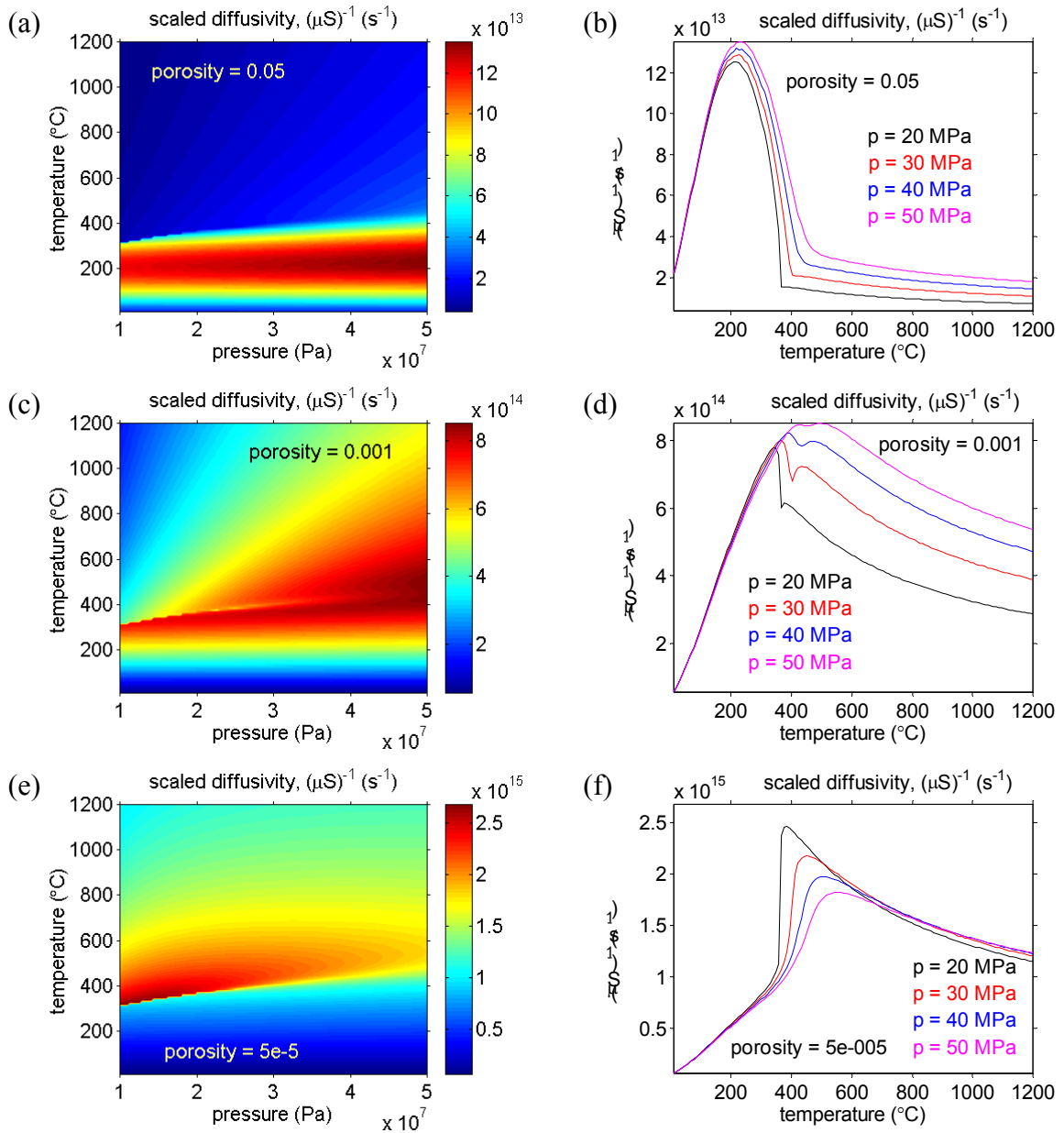


Figure 6.5: The dependence of the scaled diffusivity ($(\mu S)^{-1}$) on the thermodynamic state of the interstitial fluid in the large, intermediate and small porosity regimes with $K_g = 50$ GPa, $K_m = 30$ GPa. (The true diffusivity, in $m^2 \cdot s^{-1}$ is $k \cdot (\mu S)^{-1}$). The interstitial fluid is assumed to be pure water. Thermodynamic data from the tables embedded in the HYDROTHERM code. (a),(b) $\phi_0 = 0.05$ (large). (c),(d) $\phi_0 = 0.001$ (intermediate). (e),(f) $\phi_0 = 0.00005$ (small). (10^7 Pa corresponds to 1 km below sea level.)

Figure 6.5 shows how the scaled diffusivity depends on pressure and temperature in each of the three porosity regimes for $K_g = 50$ GPa and $K_m = 30$ GPa. In the large porosity regime - when $(\phi_0 / \phi_c) > 1$ - equations (6.7) and (6.17) imply that:

$$\frac{1}{\mu S} \approx [\phi_0] \frac{K_f}{\mu} \quad (6.18)$$

Consequently the diffusivity is proportional to (K_f / μ) (Figures 6.5a,b), and is maximised at $\sim 200^\circ\text{C}$ for seafloor pressures.

Conversely, in the small porosity regime - when $(\phi_0 / \phi_c) > 1$ - equations (6.8) and (6.17) imply that:

$$\frac{1}{\mu S} \approx \left[\frac{K_m}{\alpha} \right] \frac{1}{\mu} \quad (6.19)$$

Consequently, the diffusivity is proportional to the inverse viscosity (μ^{-1}) (Figures 6.5e,f), and is maximised at $\sim 400^\circ\text{C}$ for seafloor pressures.

In summary, Figure 6.5 shows that the scaled diffusivity is maximised somewhere between $\sim 200^\circ\text{C}$ and $\sim 400^\circ\text{C}$ for all seafloor pressures, depending on the value of the porosity. Hence, assuming that crustal permeability is homogeneous, diffusive incremental pore pressures due to tidal loading will tend to propagate furthest in regions of a subseafloor convection cell where the temperature is between $\sim 200^\circ\text{C}$ and $\sim 400^\circ\text{C}$.

Equations (6.16) and (6.17) show that the propagation of incremental pore pressure is described by a diffusion equation with diffusivity κ . When tidal loading is applied to the seafloor at angular frequency ω , diffusion occurs over a characteristic lengthscale known as the skindepth (d) defined by:

$$d = \sqrt{\frac{2\kappa}{\omega}} = \sqrt{k} \sqrt{\frac{2}{\omega}} \sqrt{\frac{1}{\mu S}} \quad (6.20)$$

It has already been remarked that the crustal permeability (k) is very poorly constrained for seafloor hydrothermal systems. Nonetheless, using equation (6.20) it is possible to make some general deductions concerning the magnitude of the skindepth (d). Figure 6.6 shows how the skindepth for semi-diurnal loading ($\omega = 1.4 \cdot 10^{-4} \text{ s}^{-1}$) depends on permeability for typical values of $(\mu S)^{-1}$ taken from Figure 6.5. In broad terms, the minimum plausible skindepth for a semi-diurnal tidal signal in seafloor crust is $d \sim 1 \text{ m}$ when $k = 10^{-17} \text{ m}^2$ and the fluid is at $\sim 2^\circ\text{C}$. Conversely, the maximum plausible skindepth is $d \sim 10,000 \text{ m}$ when $k = 10^{-10} \text{ m}^2$ and the fluid is at $\sim 400^\circ\text{C}$. It is important to note that this range of skindepths spans a very wide range. A skindepth of 1 m is very much less than the typical dimensions of a seafloor convection cell ($H \sim 1000 \text{ m}$, $L \sim 500 \text{ m}$) while a skindepth of 10,000 m is considerably larger. The dependence of the skindepth on angular frequency (ω) in equation

(6.20) implies that the skindepths for diurnal components are greater than those for semi-diurnal components by a factor of $\sqrt{2}$.

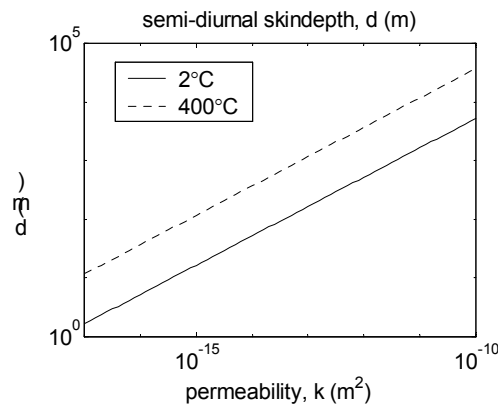


Figure 6.6: The variation of the skindepth (d) for semi-diurnal tidal loading as a function of permeability, k . Using the values from Figure 6.5c,d it is assumed that $(\mu S)^{-1}=2 \cdot 10^{-13} \text{ s}^{-1}$ at $\sim 2^\circ\text{C}$, and $(\mu S)^{-1}=10^{-15} \text{ s}^{-1}$ at 400°C . Note the logarithmic scales on both axes.

It is now possible to describe qualitatively the nature of solutions of equation (6.16) in a seafloor under tidal loading, according to the size of the skindepth (d). By considering the case of a layered seafloor, Wang & Davis (1996) demonstrated that a diffusive pressure signal is induced wherever there is a sharp contrast in the elastic properties of the seafloor. In the case of the idealised convection cell of Chapter 5, there are two such sharp boundaries in elastic properties—the seafloor itself, and the boundary separating liquid-like water from gas-like water which is approximated by the 400°C isotherm. The amplitude of the diffusive pressure signal decays exponentially over a lengthscale d away from the boundaries in elastic properties. In fact at distances greater than $2d$ from these boundaries, the diffusive pressure signal is negligible and the solution is dominated by the ‘instantaneous pressure signal’:

$$\hat{p} \approx -\beta \frac{\hat{\sigma}_{kk}}{3} = \beta \hat{p}_c \quad (6.21)$$

It should be noted that the approximate solution of equation (6.21) applies at every point of the cell which is more than a distance $2d$ from a sharp boundary in elastic properties. Consequently, the magnitude of the skindepth (d) is of great importance. In regions more than a few skindepths from boundaries in elastic properties, the incremental pore pressure is in phase with the tidal loading. Therefore, if the skindepth is very small ($d < 10 \text{ m}$) the incremental pore pressure is well approximated by equation (6.21) over almost all of the

subseafloor. It follows that the incremental pore pressure will be in phase with the ocean tide over most of the cell, although its amplitude varies according to any spatial variations in the Skempton ratio (β). In contrast, if the skindepth is comparable with the lengthscales of the cell ($d > 100$ m), then the incremental pore pressure at depth is generally not in phase with the ocean tide.

In Section 6.3, these qualitative remarks above concerning the incremental pore pressure response to tidal loading are illustrated with analytical solutions and numerical simulations.

6.3 Tidal loading of the seafloor

This section is concerned with the effect of loading by the ocean tide on a poroelastic seafloor. The nature of the global ocean tide is discussed in Chapter 2, where it is illustrated with the use of cotidal maps (Figure 2.8). The area of seafloor associated with an individual hydrothermal system typically has a lengthscale of at most 1 km. This is much smaller than the typical wavelength of the ocean tide. Consequently, it is reasonable to suppose that at any time the tidal loading is uniform over the area of seafloor associated with an individual hydrothermal convection cell.

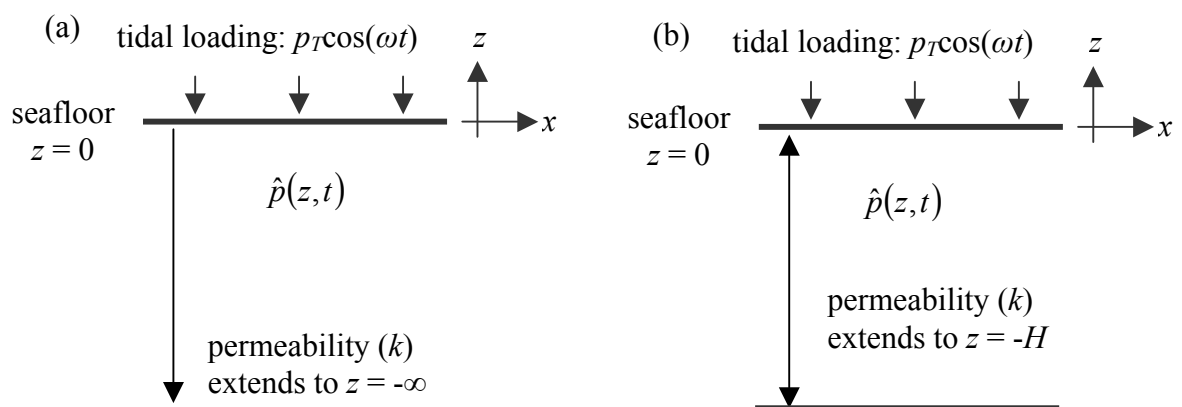


Figure 6.7: The loading of a 1-d seafloor by the ocean tide. It is supposed that there is no horizontal spatial variation. (a) Infinite 1-d halfspace. (b) Finite permeable layer of depth H .

6.3.1 Tidal loading of a 1-d seafloor

Consider the uniform tidal loading of a seafloor in which the poroelastic properties are homogeneous and the incremental pore pressure is $\hat{p}(z, t)$ (Figure 6.7a,b). Symmetry implies

that there is no horizontal strain ($\hat{e}_{11} = \hat{e}_{22} = 0$). Since the governing equations are linear, the incremental pore pressure due to a single component of the ocean tide can be considered in isolation (Table 2.1). The imposed pressure on the seafloor is therefore taken to be a time-harmonic oscillation of magnitude p_T and angular frequency ω . In complex notation, the seafloor boundary condition on the incremental pore pressure is:

$$\hat{p}(0,t) = p_T \exp(i\omega t) \quad (6.22)$$

The tides in the open oceans generally have an amplitude of ~ 1 m (Figure 2.8), and so p_T typically has an amplitude of about 10 kPa.

6.3.1.1 Incremental pore pressure in an infinite halfspace

The simplest model is one in which the permeable crust is of infinite extent below the seafloor (Figure 6.7a). The solution for this infinite halfspace is derived by Van der Kamp & Gale (1983) and is discussed in detail by Wang & Davis (1996). It is of fundamental importance, and is reproduced below.

Van der Kamp & Gale (1983) show that the incremental vertical stress is the same for all depths:

$$\hat{\sigma}_{33} = -p_T \exp(i\omega t) \quad \forall z \quad (6.23)$$

Consequently, equation (6.16) can be re-arranged to read:

$$\left[\frac{3(1-\nu)k}{(3(1-\nu) - 2\alpha\beta(1-2\nu))\mu S} \right] \frac{\partial^2 \hat{p}}{\partial z^2} = \frac{\partial \hat{p}}{\partial t} + \left[\frac{(1+\nu)\beta}{3(1-\nu) - 2\alpha\beta(1-2\nu)} \right] \frac{\partial}{\partial t} (\hat{\sigma}_{33}) \quad (6.24)$$

Since $\hat{\sigma}_{33}(z,t)$ is known from equation (6.23), equation (6.24) constitutes a forced diffusion equation for the incremental pore pressure (\hat{p}).

From equation (6.24), it is possible to define a ‘1-d diffusivity’ (κ_{1d}) according to:

$$\kappa_{1d} = \left[\frac{3(1-\nu)}{3(1-\nu) - 2\alpha\beta(1-2\nu)} \right] \frac{k}{\mu S} \quad (6.25)$$

The assumption of a 1-d seafloor leads to the introduction of the dimensionless factor in square brackets, which distinguishes κ_{1d} (equation (6.25)) from κ (equation (6.17)).

Equation (6.24) also suggests the definition of a ‘1-d loading efficiency’ (γ_{1d}) according to:

$$\gamma_{1d} = \left[\frac{(1+\nu)}{3(1-\nu) - 2\alpha\beta(1-2\nu)} \right] \beta \quad (6.26)$$

The assumption a 1-d seafloor leads to the introduction of the dimensionless factor in square brackets which distinguishes γ_{1d} (equation (6.26)) from the Skempton ratio, β (equation (6.9)).

Referring to the 1-d parameters of equations (6.25) and (6.26), equation (6.24) yields an equation governing the diffusion of incremental pore pressure in a homogeneous 1-d seafloor:

$$\kappa_{1d} \frac{\partial^2 \hat{p}}{\partial z^2} = \frac{\partial \hat{p}}{\partial t} + \gamma_{1d} \frac{\partial}{\partial t} (-p_T \exp(i\omega t)) \quad (6.27)$$

By analogy with the skindepth (d) (equation (6.20)), a ‘1d-skindepth’, representing the lengthscale of diffusion of the incremental pore pressure, can be defined by:

$$d_{1d} = \sqrt{\frac{2\kappa_{1d}}{\omega}} \quad (6.28)$$

Since κ_{1d} and γ_{1d} are not here functions of space, equations (6.22) and (6.27) have the (complex) solution:

$$\hat{p}(z, t) = p_T \left[(1 - \gamma_{1d}) \exp\left(\left(\frac{1+i}{d_{1d}}\right)z\right) + \gamma_{1d} \right] \exp(i\omega t) \quad (6.29)$$

Equation (6.29) can be written in real notation as:

$$\hat{p}(z, t) = p_T \left[(1 - \gamma_{1d}) \exp\left(\frac{z}{d_{1d}}\right) \cos\left(\frac{z}{d_{1d}} + \omega t\right) + \gamma_{1d} \cos(\omega t) \right] \quad (6.30)$$

Typical depth profiles associated with this solution are shown in Figure 6.8. It is conceptually useful to split the solution of equation (6.30) into the sum of an instantaneous signal ($p_T \gamma_{1d} \cos(\omega t)$) and a diffusive signal ($p_T (1 - \gamma_{1d}) \exp(z/d_{1d}) \cos(z/d_{1d} + \omega t)$). The instantaneous signal is in phase with the ocean tide and has magnitude $p_T \gamma_{1d}$ for all depths. In contrast, the diffusive signal decays exponentially from the seafloor over a lengthscale d_{1d} and is generally not in phase with the ocean tide. Figure 6.8 shows that the nature of the incremental pore pressure solution depends on the value of z/d_{1d} . Close to the seafloor (i.e. within one or two skindepths) the incremental pore pressure contains a significant diffusive component. Further from the seafloor, however, the incremental pore pressure is dominated by the instantaneous signal ($p_T \gamma_{1d} \cos(\omega t)$). Therefore the 1-d loading efficiency (γ_{1d}) represents the proportion of the tidal load which is borne by the interstitial fluid at depths greater than 2 skindepths.

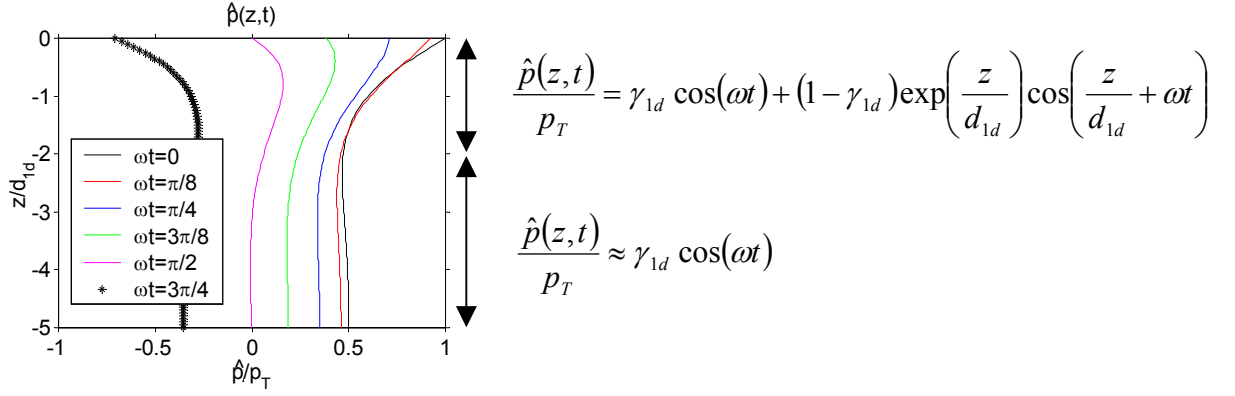


Figure 6.8: Typical depth profiles of the incremental pore pressure ($\hat{p}(z,t)$) as a function of dimensionless depth ($-z/d_{1d}$) in an infinite halfspace at various times during the tidal cycle with $\gamma_{1d} = 0.5$. High tide occurs when $\omega t = 0$. Half tide occurs when $\omega t = \pi/2$. Maximum vertical velocity at the seafloor occurs when $\omega t = 3\pi/4$. The diffusive pressure signal is limited to depths for which $(-z/d_{1d}) < \sim 2$.

6.3.1.2 Incremental velocity in an infinite halfspace

Previous authors have been concerned solely with the incremental pore pressure (Van der Kamp & Gale, 1983; Wang & Davis, 1996). In contrast, the aim here is to investigate the flow of interstitial fluids induced by the incremental pore pressure. In other words, the point of interest is the *spatial gradient* of the incremental pore pressure rather than the incremental pore pressure itself. The tidally induced incremental velocity at the seafloor ($z = 0$) is of particular interest since it can be measured by instruments such as Medusa (Chapter 4).

Applying Darcy's law to equation (6.29), the incremental vertical velocity (in complex notation) is:

$$\hat{w}(z,t) = -\frac{k}{\mu} \frac{\partial \hat{p}}{\partial z} = -\frac{k}{\mu} p_T (1 - \gamma_{1d}) \left(\frac{1+i}{d_{1d}} \right) \exp\left(\left(\frac{1+i}{d_{1d}} \right) z + i\omega t \right) \quad (6.31)$$

Therefore the tidally induced incremental velocity at the seafloor is:

$$\hat{w}(0,t) = -\frac{k}{\mu} p_T (1 - \gamma_{1d}) \left(\frac{1+i}{d_{1d}} \right) \exp(i\omega t) \quad (6.32)$$

Equation (6.32) shows that the tidally induced outflow of water at the seafloor *leads* the ocean tide by a radian angle $\arg(-(1+i)) = -3\pi/4$ radians. In other words, the tidally induced outflow of pore water at the seafloor *lags* the ocean tide by $+3\pi/4$ radians (or 135°). Therefore peak outflow occurs $\sim 4\frac{1}{2}$ hours after high tide for the semi-diurnal components,

and ~9 hours after high tide for diurnal components. In principle, this predicted phase lag of 135° could be compared with observed effluent velocity time-series from the seafloor for each harmonic component of the tide (Table 2.1). However, the effluent velocity time-series which have been collected to date are too short and too noisy to allow the extraction of individual harmonic components (Chapter 4). Comparison of this theory with observation will therefore have to await the collection of higher quality data.

The tidally modulated effluent velocities observed on the seafloor take the form of a small incremental velocity (\hat{w}) imposed on a steady background flow (w). From equation (6.32), the amplitude of the velocity variations is:

$$|\hat{w}| = \frac{p_T k (1 - \gamma_{1d})}{\mu d_{1d}} \quad (6.33)$$

Assuming that the background flow consists of fluid of density ρ ascending a cold hydrostatic pressure gradient ($g\rho_0$), the steady velocity (w) is given by:

$$w = \frac{gk(\rho_0 - \rho)}{\mu} \quad (6.34)$$

From equations (6.33) and (6.34), it is possible to define the dimensionless magnitude of the incremental seafloor velocity as follows:

$$\frac{|\hat{w}|}{w} = \left(\frac{p_T}{g} \right) \frac{(1 - \gamma_{1d})}{(\rho_0 - \rho)d_{1d}} \quad (6.35)$$

Equation (6.35) expresses the magnitude of the tidal oscillations in effluent velocity as a fraction of the background steady velocity. Using the fact that $S = \alpha / (K_m \beta)$, and equations (6.25), (6.26) and (6.28), it can be shown that:

$$d_{1d} = \frac{1}{\sqrt{\omega}} \sqrt{k} \sqrt{\frac{6K_m(1-\nu)}{\alpha(1+\nu)}} \sqrt{\frac{\gamma_{1d}}{\mu}} \quad (6.36)$$

Equations (6.35) and (6.36) then imply that the dimensionless magnitude of the incremental seafloor velocity is:

$$\frac{|\hat{w}|}{w} = \underbrace{\left[\frac{p_T}{g} \sqrt{\frac{\alpha(1+\nu)}{6K_m(1-\nu)}} \right]}_{(a)} \cdot \underbrace{\left[\sqrt{\omega} \right]}_{(b)} \cdot \underbrace{\left[\frac{1}{\sqrt{k}} \right]}_{(c)} \cdot \underbrace{\left[\frac{\sqrt{\mu}(1-\gamma_{1d})}{(\rho_0 - \rho)\sqrt{\gamma_{1d}}} \right]}_{(d)} \quad (6.37)$$

The terms in square brackets in equation (6.37) can be considered in turn, to reveal how variations in parameter values affect the magnitude of the velocity perturbations observed at the seafloor. Term (a) contains quantities which are either fixed constants or elastic parameters of the rock matrix, while term (b) shows that the dimensionless incremental velocity increases with the frequency of the loading. Consequently, under this theory,

seafloor velocity signals are predicted to be *high-pass filtered* relative to the ocean tide. Equation (6.37) predicts that the ratio of semi-diurnal to diurnal amplitudes in the outflow velocity signal is greater than that in the ocean tide by a factor of $\sqrt{2}$. Term (c) shows that the dimensionless magnitude of the incremental velocity decreases as the permeability increases. Term (d) reveals the dependence of the velocity perturbations on the thermodynamic state of the pore water and can be used to define a ‘tidal flow magnitude parameter’ (M_T) as follows:

$$M_T = \left[\frac{(1 - \gamma_{1d})}{\sqrt{\gamma_{1d}}} \right] \frac{\sqrt{\mu}}{(\rho_0 - \rho)} \quad (6.38)$$

Graphs of M_T are presented in Figure 6.9 over a range of p - T conditions appropriate to hydrothermal systems. When the porosity (ϕ_0) is very small, $\gamma_{1d} \approx 1$ and so:

$$M_T \approx \frac{\sqrt{\mu}}{(\rho_0 - \rho)} \quad (6.39)$$

Figure 6.9 shows that M_T is minimised at $\sim 400^\circ\text{C}$ for all seafloor pressures. Hence, the ratio of the tidally induced incremental velocity to the buoyancy driven background velocity is a *decreasing* function of temperature for the temperatures below $\sim 400^\circ\text{C}$ which characterise the discharge zone of a subsurface convection cell (Chapter 5). Therefore equations (6.37) and (6.38) predict that the tidal variations in effluent velocity are most significant as a fraction of the steady flow for:

- (1) cool effluent
- (2) high frequency loading
- (3) low permeabilities

The observation that effluent velocity variations are greatest for high frequency loading implies that the relative magnitudes of semi-diurnal to diurnal components will be greater in an effluent velocity time-series than in the local ocean tide. It has already been remarked (Chapter 2) that the semi-diurnal components of the ocean tide are typically larger than the diurnal components. For these two reasons, it is expected that tidal variations in effluent velocity will, in general, be dominated by semi-diurnal frequencies. In the subsequent sections it is assumed for simplicity that the load at the seafloor is a pure sine wave of angular frequency ω . By linearity, the diurnal and semi-diurnal components may be considered separately. In the case of semi-diurnal loading $\omega = 1.408 \cdot 10^{-4} \text{ rad.s}^{-1}$, while for diurnal loading $\omega = 7.038 \cdot 10^{-5} \text{ rad.s}^{-1}$.

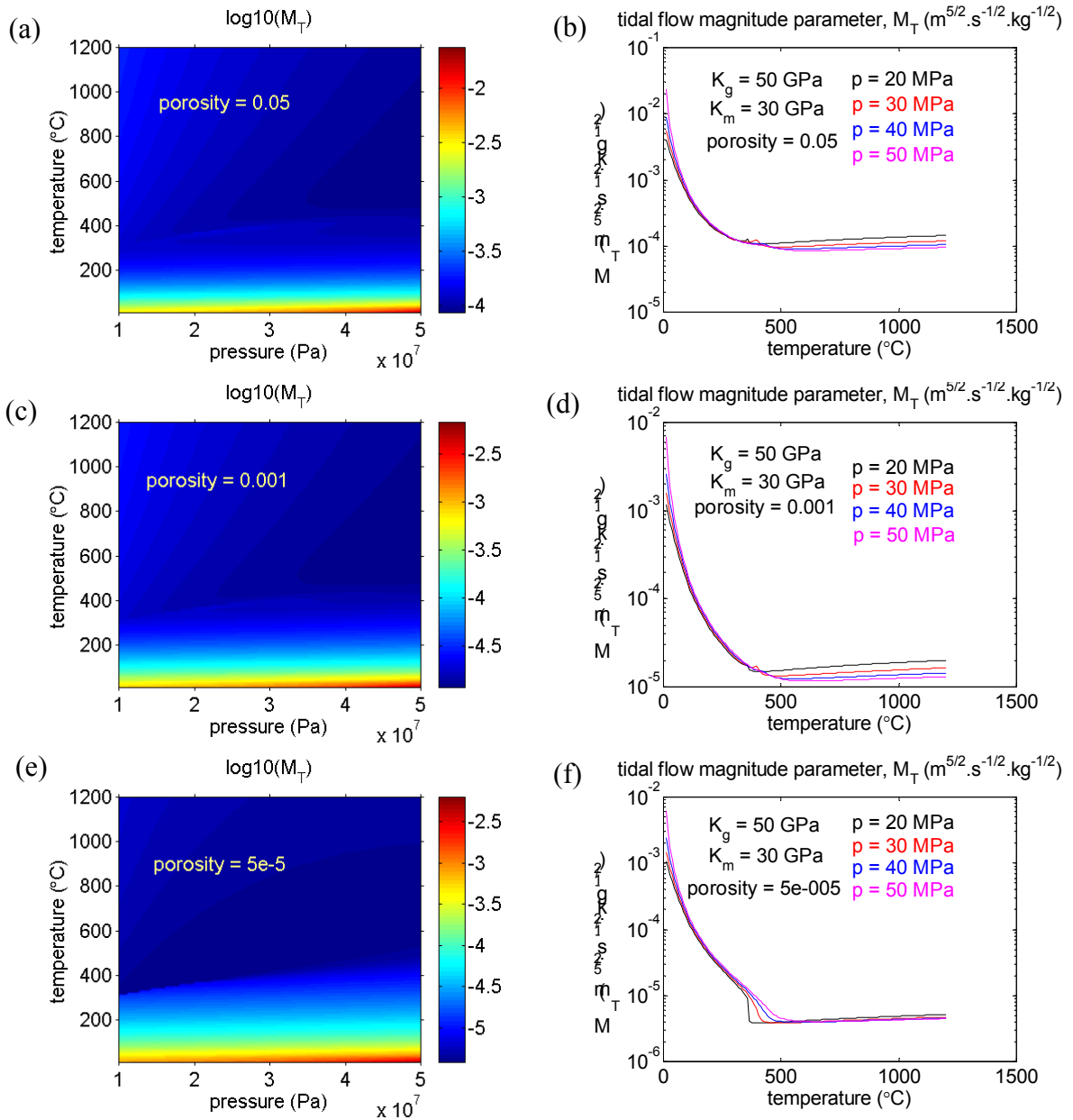


Figure 6.9: The dependence of the tidal flow magnitude parameter (M_T) on the thermodynamic state of the interstitial fluid in the large, intermediate and small porosity regimes with $K_g = 50$ GPa, $K_m = 30$ GPa. The magnitude of the velocity perturbations at the seafloor, relative to the background velocity, is proportional to M_T . Interstitial fluid is pure water. Thermodynamic data from the tables embedded in the HYDROTHERM code. (a), (b) $\phi_0 = 0.05$ (large). (c), (d) $\phi_0 = 0.001$ (intermediate). (e), (f) $\phi_0 = 0.00005$ (small). (10⁷ Pa corresponds to 1 km below sea level.)

6.3.1.3 Incremental temperature in an infinite halfspace

In the previous section, the incremental pore pressure solution of Van der Kamp & Gale (1983) ($\hat{p}(z,t)$) is extended to yield an expression for the incremental velocity ($\hat{w}(z,t)$). In this section, an expression for a third quantity of interest - the incremental temperature ($\hat{T}(z,t)$) - is derived.

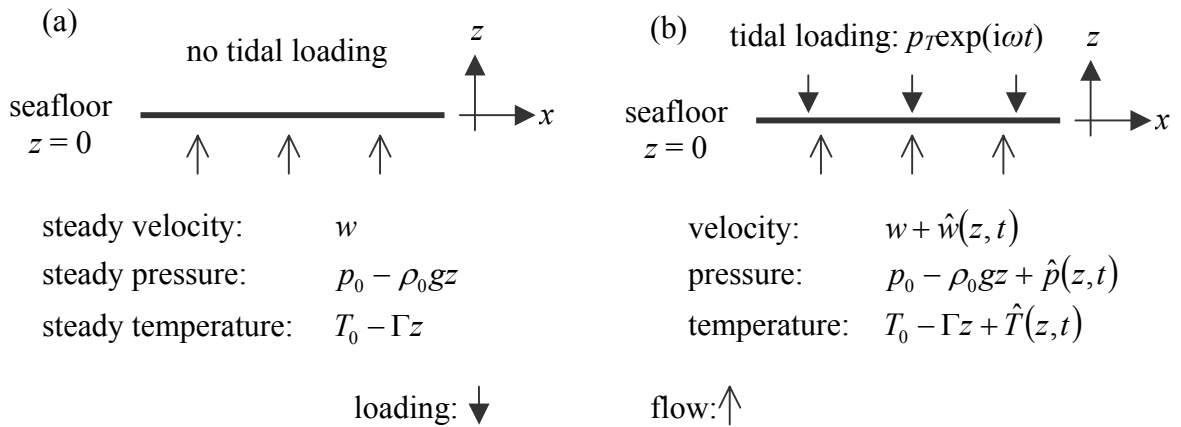


Figure 6.10: The incremental temperature ($\hat{T}(z,t)$) due to tidal loading, just below the seafloor. (a) In the absence of tidal loading, the vertical velocity is assumed to be constant while the pressure and temperature are linear functions of depth. (b) Under tidal loading, the pressure, velocity and temperature are all tidally modulated.

For simplicity, it is supposed that pressure and temperature are linear functions of depth in the absence of tidal loading (Figure 6.10a). This is approximately true in the section of the hydrothermal discharge zone which lies just below the seafloor (Figure 5.1). If the pressure gradient is cold hydrostatic (Section 5.3) and the temperature gradient is denoted by Γ , then:

$$p(z) = p_0 - g\rho_0 z \quad (6.40)$$

$$T(z) = T_0 - \Gamma z \quad (6.41)$$

It is supposed for simplicity that the density (ρ) and dynamic viscosity (μ) do not vary with depth. The buoyancy-driven vertical velocity (in the absence of tidal loading) therefore has the constant value:

$$w = \frac{-k}{\mu} \left[\frac{dp}{dz} + g\rho \right] = \frac{gk(\rho_0 - \rho)}{\mu} \quad (6.42)$$

This steady state flow (Figure 6.10a) satisfies mass conservation because:

$$\frac{\partial}{\partial z}(\rho w) = 0 \quad (6.43)$$

However, the advective energy accumulation per unit volume (Q) is non-zero because:

$$Q = -\frac{\partial}{\partial z}(\rho h w) = -\rho w \frac{\partial h}{\partial z} \quad (6.44)$$

Supposing for simplicity that enthalpy is a linear function of temperature - $h(p, T) = c_p T$ - it then follows that:

$$Q = \rho c_p w \Gamma \quad (6.45)$$

In a real seafloor system, the advective energy accumulation of equation (6.45) would be balanced by the lateral conductive flow of heat away from the discharge zone. It is not possible to incorporate lateral conduction into this model explicitly because it is assumed that there is only one spatial dimension. However, energy can be balanced by assuming that heat is removed at a rate Q per unit volume at all depths below the seafloor. In other words, heat sinks must be introduced to simulate the effect of conductive heat loss and ensure that energy is balanced in the steady state.

It is supposed that the steady, one-dimensional solution described above is disturbed by tidal loading ($p_T \exp(i\omega t)$) on the seafloor ($z = 0$) (Figure 6.10b). The pressure, velocity and temperature are then perturbed from their steady values as follows:

$$\begin{aligned} p(z) &\rightarrow p_0 - g\rho_0 z + \hat{p}(z, t) \\ w &\rightarrow w + \hat{w}(z, t) \\ T(z) &\rightarrow T_0 - \Gamma z + \hat{T}(z, t) \end{aligned} \quad (6.46)$$

Assuming that the incremental pressure ($\hat{p}(z, t)$) and incremental velocity ($\hat{w}(z, t)$) are given by the 1-d solutions discussed in previous sections (equations (6.29) and (6.31)), an expression for the incremental temperature ($\hat{T}(z, t)$) can be derived.

If tidally induced changes in fluid density are negligible, the conservation of energy under tidal loading is expressed by the advection-diffusion equation:

$$\frac{\partial}{\partial t}(T + \hat{T}) + (w + \hat{w}) \frac{\partial}{\partial z}(T + \hat{T}) = -\frac{Q}{\rho c_p} \quad (6.47)$$

Equation (6.47) can be linearised by neglecting the product of any two incremental properties. Using equations (6.41) and (6.45), this linearisation yields:

$$\frac{\partial \hat{T}}{\partial t} + w \frac{\partial \hat{T}}{\partial z} = \Gamma \hat{w} \quad (6.48)$$

The steady state velocity (w) and the steady state temperature gradient (Γ) are both constant. Therefore equation (6.48) can be used to derive an expression for the incremental temperature ($\hat{T}(z,t)$) in terms of the incremental velocity ($\hat{w}(z,t)$). Equation (6.31) shows that the tidally induced incremental velocity has the form:

$$\hat{w}(z,t) = A \exp\left(\left(\frac{1+i}{d_{1d}}\right)z + i\omega t\right) \quad (6.49)$$

where A is a complex number expressing the amplitude and the phase relative to the ocean tide.

Equation (6.48) suggests that the incremental temperature has a similar form to equation (6.49). Accordingly, it is postulated that:

$$\hat{T}(z,t) = B \exp\left(\left(\frac{1+i}{d_{1d}}\right)z + i\omega t\right) \quad (6.50)$$

where the value of the unknown complex constant (B) remains to be calculated.

Equations (6.48), (6.49) and (6.50) together yield an expression linking the complex amplitudes A and B :

$$B \frac{w}{d_{1d}} \left[1 + \left(1 + \frac{\omega d_{1d}}{w}\right)i\right] = \Gamma \cdot A \quad (6.51)$$

Equation (6.51) shows that the incremental temperature ($\hat{T}(z,t)$) lags the incremental velocity ($\hat{w}(z,t)$) by the radian angle:

$$\arg(A) - \arg(B) = \arg\left[1 + \left(1 + \frac{\omega d_{1d}}{w}\right)i\right] \quad (6.52)$$

Since ω , d_{1d} , and w are all positive real numbers, equation (6.52) implies that the incremental temperature lags the incremental velocity by an angle in the range $[\pi/4, \pi/2]$ (i.e. between 45° and 90°). The exact value of this phase lag depends on the value of the dimensionless parameter:

$$\frac{\omega d_{1d}}{w} = \left[\frac{1}{g(\rho_0 - \rho)} \sqrt{\frac{2\omega\mu}{S}} \sqrt{\frac{3(1-\nu)}{3(1-\nu) - 2\alpha\beta(1-2\nu)}} \right] \frac{1}{\sqrt{k}} \quad (6.53)$$

For semi-diurnal tidal loading, $\omega = 1.4 \cdot 10^{-4} \text{ s}^{-1}$ and all parameters except the permeability (k) are known accurately. Assuming typical values ($g = 9.8 \text{ m.s}^{-2}$, $(\rho_0 - \rho) = 500 \text{ kg.m}^{-3}$, $\mu = 5 \cdot 10^{-5} \text{ Pa.s}$, $S = 5 \cdot 10^{-9} \text{ Pa}^{-1}$, $\nu = 0.2$, $\alpha = 0.5$, $\beta = 0.5$), suggests that, in SI units:

$$\frac{\omega d_{1d}}{w} \approx 7 \cdot 10^{-4} \frac{1}{\sqrt{k}} \quad (6.54)$$

Using equations (6.52) and (6.54), the phase difference between the incremental velocity and the incremental temperature can be graphed as a function of permeability (k) (Figure 6.11). Table 6.1 suggests that the permeability of the seafloor lies between 10^{-17} m^2 and 10^{-10} m^2 . Figure 6.11 shows that the incremental temperature lags the incremental velocity by almost exactly 90° within this range. Phase lags significantly smaller than 90° are only possible for permeabilities greater than 10^{-9} m^2 . Such high permeabilities could only exist if there were considerable cracking of the discharge zone. Consequently, seafloor measurements of the phase lag between effluent velocity and temperature are diagnostic. Phase lags significantly below 90° present evidence for unusually high seafloor permeability.

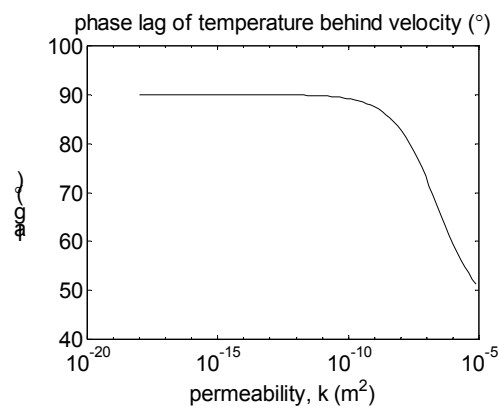


Figure 6.11: The predicted phase lag of the incremental temperature ($\hat{T}(z,t)$) behind the incremental velocity ($\hat{w}(z,t)$) as a function of permeability (k) for typical seafloor parameter values. Note the logarithmic scale on the horizontal axis.

In the infinite halfspace model, it has been shown that the incremental velocity at the seafloor lags the ocean tide by 135° . Consequently, the infinite halfspace model predicts that the incremental temperature at the seafloor lags the ocean tide by an angle in the range $[180^\circ, 225^\circ]$. Furthermore, for semi-diurnal loading and permeabilities less than 10^{-10} m^2 , the phase lag is predicted to be almost exactly equal to 225° (Figure 6.11).

6.3.1.4 Incremental pore pressure in a finite permeable layer

The assumption of an infinite halfspace is a significant simplification, and it is of interest to extend the well-established halfspace model of Van der Kamp & Gale (1983) to the case of a

finite permeable layer. It is therefore supposed in this section that the crust is only permeable between $z = 0$ and $z = -H$ (Figure 6.6b).

The new boundary condition ($\hat{w}(-H, t) = 0$) means that the solution of equation (6.27), which is given by equation (6.29) for an infinite halfspace, is now given by:

$$\hat{p}(z, t) = p_T \left[\frac{\cosh\left((1+i)\left(\frac{z+H}{d_{1d}}\right)\right)}{\cosh\left((1+i)\left(\frac{H}{d_{1d}}\right)\right)} + \gamma_{1d} \right] \exp(i\omega t) \quad (6.55)$$

6.3.1.5 Incremental velocity in a finite permeable layer

By Darcy's law, it follows from equation (6.55) that the incremental velocity for a finite permeable layer is given (in complex notation) by:

$$\hat{w}(z, t) = -\frac{k}{\mu} p_T (1 - \gamma_{1d}) \frac{(1+i)}{d_{1d}} \frac{\sinh\left((1+i)\left(\frac{z+H}{d_{1d}}\right)\right)}{\cosh\left((1+i)\left(\frac{H}{d_{1d}}\right)\right)} \exp(i\omega t) \quad (6.56)$$

The incremental velocity on the seafloor is then:

$$\hat{w}(0, t) = -\frac{k}{\mu} p_T (1 - \gamma_{1d}) \frac{(1+i)}{d_{1d}} \tanh\left((1+i)\left(\frac{H}{d_{1d}}\right)\right) \exp(i\omega t) \quad (6.57)$$

It should be noted that the presence of the impermeable boundary at $z = -H$ affects both the magnitude and phase of the outflow at the seafloor (equation (6.57)), compared with the solution for an infinite halfspace (equation (6.32)).

It can be shown that:

$$\left| \tanh\left((1+i)\left(\frac{H}{d_{1d}}\right)\right) \right| = \sqrt{\frac{\sinh^2\left(\frac{H}{d_{1d}}\right) + \sin^2\left(\frac{H}{d_{1d}}\right)}{\sinh^2\left(\frac{H}{d_{1d}}\right) + \cos^2\left(\frac{H}{d_{1d}}\right)}} \quad (6.58)$$

and that:

$$\arg\left[\tanh\left((1+i)\left(\frac{H}{d_{1d}}\right)\right)\right] = \tan^{-1}\left[\frac{\sin\left(\frac{2H}{d_{1d}}\right)}{\sinh\left(\frac{2H}{d_{1d}}\right)}\right] \quad (6.59)$$

Therefore the tidally induced outflow at the seafloor has magnitude:

$$\frac{p_T k (1 - \gamma_{1d})}{\mu d_{1d}} \sqrt{\frac{\sinh^2\left(\frac{H}{d_{1d}}\right) + \sin^2\left(\frac{H}{d_{1d}}\right)}{\sinh^2\left(\frac{H}{d_{1d}}\right) + \cos^2\left(\frac{H}{d_{1d}}\right)}} \quad (6.60)$$

It has already been shown (equation (6.32)) that the effluent velocity at the seafloor lags the ocean tide by a radian angle ($3\pi / 4$) in the case of an infinite halfspace. It follows from equation (6.59) that the presence of an impermeable boundary at $z = -H$ means that the effluent velocity at the seafloor lags the ocean tide by a radian angle:

$$\frac{3\pi}{4} - \tan^{-1} \left[\frac{\sin\left(\frac{2H}{d_{1d}}\right)}{\sinh\left(\frac{2H}{d_{1d}}\right)} \right] \quad (6.61)$$

The predicted magnitude (equation (6.60)) and phase lag (equation (6.61)) of the incremental velocity at the seafloor are shown in Figure 6.12 as functions of the dimensionless depth of the impermeable boundary (H / d_{1d}).

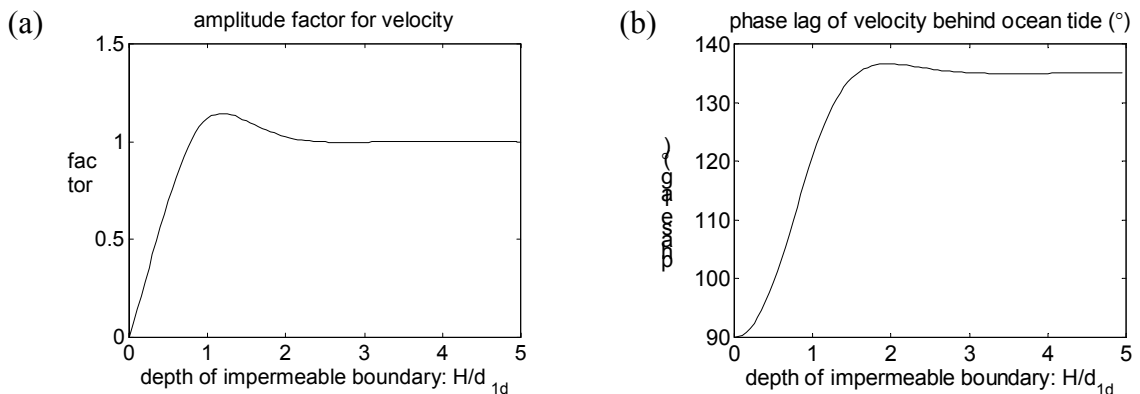


Figure 6.12: The effect of an impermeable layer at depth H on the magnitude and phase of the incremental velocity at the seafloor. The horizontal axes measure the dimensionless depth of the impermeable layer (H/d_{1d}). (a) The amplitude of the outflow as a fraction of the infinite halfspace solution, which is approached as $H/d_{1d} \rightarrow \infty$. (b) The lag of the outflow behind the ocean tide in degrees, which approaches the infinite halfspace value of 135° as $H/d_{1d} \rightarrow \infty$.

In summary, the incremental velocity at the seafloor lags the ocean tide by an angle between 90° and 135° , depending on the relative magnitude of the 1-d skindepth (d_{1d}) and depth over which the seafloor crust is permeable (H). If the skindepth is much smaller than the thickness of the permeable layer ($H / d_{1d} \gg 1$) the incremental velocity follows the infinite halfspace solution and lags the ocean tide by 135° . In contrast, if the skindepth is greater than $H/2$ (so that $H / d_{1d} < 1$), then the incremental velocity at the seafloor is reduced in magnitude compared to the infinite halfspace solution (Figure 6.12a), and its phase lag behind the ocean tide takes a value in the range $[90^\circ, 135^\circ]$. When sufficient high quality data are available, observed values of the phase lag between the ocean tide and the effluent could be used to constrain the ratio (H / d_{1d}).

6.3.2 Tidal loading of a 2-d seafloor

In Section 6.3.1, the investigation of tidal loading is restricted to one spatial dimension for simplicity. In this section, the same principles are extended to two dimensions by considering the tidal loading of the simulated convection cell of Chapter 5. The numerical steady state solution (Figure 5.4) defines the properties of the interstitial fluid as functions of space. Figure 6.13 shows the distribution of pressure (p), temperature (T), density (ρ) and fluid compressibility (K_f^{-1}) within the simulated convection cell. It should be noted that the seafloor is placed at $z = 0$ m in these figures in common with the convention followed throughout this chapter. (In Chapter 5, however, it is more convenient to place the seafloor at $z = 1000$ m). The division between the cold, dense, liquid-like region below $\sim 400^\circ\text{C}$ and the hot, buoyant, gas-like region above $\sim 400^\circ\text{C}$ is clearly shown in Figure 6.13c,d. Under tidal loading, it is expected that the differing incremental pore pressures in these regions will drive a tidally modulated flow. In the following sections, a numerical simulation is used to examine this flow.

6.3.2.1 Governing equations in 2-d

In Section 6.3.1.1 the equations governing the propagation of incremental pore pressure in one dimension are derived (Van der Kamp & Gale, 1983). In this section, the analogous equations governing the incremental stress ($\hat{\sigma}_{ij}(x, z, t)$) and incremental pore pressure ($\hat{p}(x, z, t)$) in two spatial dimensions are derived. In this case, the assumption of only two spatial dimensions implies that $\hat{e}_{22} = 0$. Therefore equations (6.12) and (6.13) imply that:

$$\hat{\sigma}_{kk} = (1 + \nu)(\hat{\sigma}_{11} + \hat{\sigma}_{33}) - \alpha(1 - 2\nu)\hat{p} \quad (6.62)$$

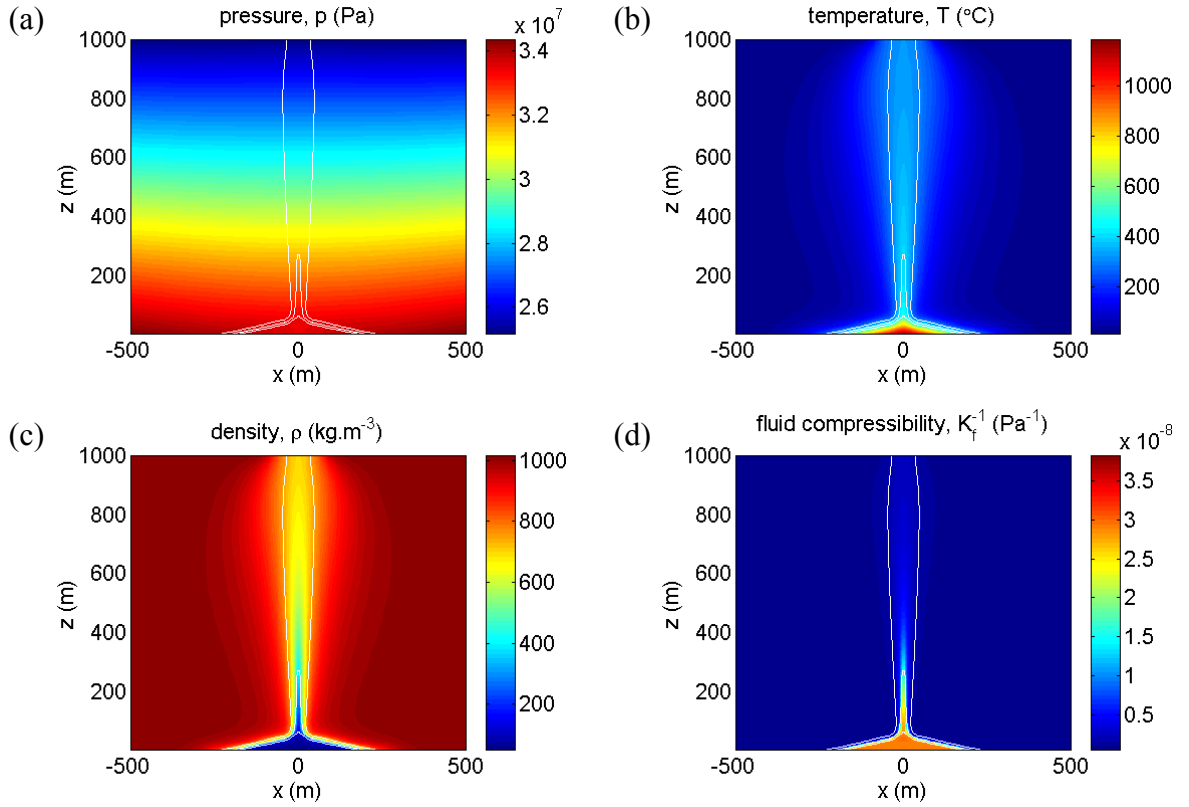


Figure 6.13: The thermodynamic properties of the fluid in the numerically simulated convection cell of Section 5.3. In each plot, the domain is the same as that shown in Figure 5.4a. The seafloor is at $z = 0$ m and a magma chamber lies at $z = -1000$ m. On all plots the isotherms at 300°C , 400°C and 500°C are shown in white. The change from liquid-like properties to gas-like properties occurs at $\sim 400^\circ\text{C}$. (a) The pore pressure, p . (b) The temperature, T . (c) The density, ρ . (d) The fluid compressibility, K_f^{-1} .

It then follows from equation (6.14) that:

$$\alpha(1-2\nu)\left[\frac{\partial^2}{\partial x^2} + \frac{\partial^2}{\partial z^2}\right]\hat{p} + \left[(2-\nu)\frac{\partial^2}{\partial x^2} + (1-\nu)\frac{\partial^2}{\partial z^2}\right]\hat{\sigma}_{11} + \left[(1-\nu)\frac{\partial^2}{\partial x^2} - \nu\frac{\partial^2}{\partial z^2}\right]\hat{\sigma}_{33} = 0 \quad (6.63)$$

$$\alpha(1-2\nu)\left[\frac{\partial^2}{\partial x^2} + \frac{\partial^2}{\partial z^2}\right]\hat{p} + \left[-\nu\frac{\partial^2}{\partial x^2} + (1-\nu)\frac{\partial^2}{\partial z^2}\right]\hat{\sigma}_{11} + \left[(1-\nu)\frac{\partial^2}{\partial x^2} + (2-\nu)\frac{\partial^2}{\partial z^2}\right]\hat{\sigma}_{33} = 0 \quad (6.64)$$

Equation (6.16) implies that:

$$\left[\frac{3k}{(3-\alpha\beta(1-2\nu))\mu S}\right]\frac{\partial^2 \hat{p}}{\partial z^2} = \frac{\partial \hat{p}}{\partial t} + \left[\frac{(1+\nu)\beta}{3-\alpha\beta(1-2\nu)}\right]\frac{\partial}{\partial t}(\hat{\sigma}_{11} + \hat{\sigma}_{33}) \quad (6.65)$$

Equation (6.65) suggests the definition of a 2-d diffusivity according to:

$$\kappa_{2d} = \left[\frac{3}{3 - \alpha\beta(1 - 2\nu)} \right] \frac{k}{\mu S} \quad (6.66)$$

and a 2-d loading efficiency according to:

$$\gamma_{2d} = \left[\frac{(1 + \nu)}{3 - \alpha\beta(1 - 2\nu)} \right] \beta \quad (6.67)$$

It then follows that conservation of fluid mass is expressed by:

$$\kappa_{2d} \frac{\partial^2 \hat{p}}{\partial z^2} = \frac{\partial \hat{p}}{\partial t} + \gamma_{2d} \frac{\partial}{\partial t} (\hat{\sigma}_{11} + \hat{\sigma}_{33}) \quad (6.68)$$

Equations (6.63), (6.64) and (6.68) are the governing equations for the three scalar fields $\hat{p}(x, z, t)$, $\hat{\sigma}_{11}(x, z, t)$ and $\hat{\sigma}_{33}(x, z, t)$. A numerical solution for these fields can be found when tidal loading ($p_T \cos(\omega t)$) is applied to the seafloor ($z = 0$).

6.3.2.2 Numerical simulation

Boundary conditions are required in order to obtain a numerical solution to equations (6.63), (6.64) and (6.68). Considering first the incremental pore pressure, the tidal loading on the seafloor imposes the condition:

$$\hat{p} = p_T \exp(i\omega t) \quad (z = 0) \quad (6.69)$$

The bottom boundary ($z = -1000$ m) is taken to be impermeable, which implies that:

$$\left. \frac{\partial \hat{p}}{\partial z} \right|_{z=-1000} = 0 \quad (6.70)$$

It is expected that the one dimensional solution of Section 6.3.1.1 will apply on the side boundaries ($x = \pm 500$ m). If the 1-d skindepth and 1-d loading efficiency for cold water are labelled d_c and γ_c respectively, then equation (6.27) implies the boundary conditions:

$$\hat{p}(\pm 500, z, t) = \gamma_c p_T \exp(i\omega t) + (1 - \gamma_c) p_T \exp\left(\frac{(1+i)z}{d_c} + i\omega t\right) \quad (6.71)$$

Following Van der Kamp & Gale (1983) it is assumed that the boundary condition for the vertical stress is the same on all four boundaries:

$$\sigma_{33} = -p_T \exp(i\omega t) \quad (6.72)$$

Finally, in order to ensure that $\hat{e}_{22} = 0$, the following condition must be met on all four boundaries:

$$\sigma_{11} = \frac{\nu}{1 - \nu} \sigma_{33} - \frac{\alpha(1 - 2\nu)}{1 - \nu} p \quad (6.73)$$

Since the tidal loading is assumed to occur at a single angular frequency ω , it follows that the incremental pressure and stress can be written in the form:

$$\left. \begin{aligned} \hat{p}(x, z, t) &= P(x, z) \exp(i\omega t) \\ \hat{\sigma}_{11}(x, z, t) &= \Sigma_{11}(x, z) \exp(i\omega t) \\ \hat{\sigma}_{33}(x, z, t) &= \Sigma_{33}(x, z) \exp(i\omega t) \end{aligned} \right\} \quad (6.74)$$

The governing equations (6.63), (6.64), (6.68) and the boundary conditions (6.69) – (6.73) can then be solved using standard finite difference techniques (Press *et al.*, 1986) to find the complex amplitudes $P(x, z)$, $\Sigma_{11}(x, z)$ and $\Sigma_{33}(x, z)$.

Unfortunately, only a very limited amount of computer time was available to perform calculations of this nature, and the parameters used ($K_m = 0.5$ GPa, $K_g = 50$ GPa, $\nu = 0.1$, $\varphi_0 = 0.1$, $k = 10^{-12}$ m²) are not consistent with those assumed elsewhere in this dissertation (Chapter 5). Computer facilities were not available to rerun the simulations with consistent parameter values. The results (Figures 6.14 – 6.16) should therefore be viewed as illustrative of a general principle rather than definitive. Nonetheless, the simulations cover a sufficiently wide range of parameter values to illustrate the different incremental pore pressure regimes which apply according to the size of the cold skindepth d_c . The subscript ‘c’ is used to denote the values of the loading efficiency (γ_c) and skindepth (d_c) obtained for cold water from equations (6.26) and (6.28). Similarly, the subscript ‘h’ is used to denote the values (γ_h and d_h) obtained for hot ($\sim 400^\circ\text{C}$), gas-like water. In these numerical examples, $\gamma_c \approx 0.93$ and $\gamma_h \approx 0.14$. The seafloor parameter known to the least precision is the permeability (k), which can vary over several orders of magnitude (Table 6.1). Equation (6.28) shows that cold skindepth d_c depends on the ratio (k / ω), and so the effect of varying k is simulated numerically by varying ω .

Figure 6.14 shows the calculated incremental pore pressure for tidal loading with $k = 10^{-12}$ m², $\omega = 0.1$ s⁻¹. In this case the cold skindepth ($d_c = 2.6$ m) is much smaller than the dimensions of the cell, and so the diffusive part of the incremental pore pressure is restricted to a region of lengthscale $2d_c = 5.2$ m around the seafloor and the boundary between the liquid-like and gas-like regions. At distances greater than $2d_c$ from these boundaries in elastic properties, the solution takes a form equivalent to the instantaneous pressure signal of equation (6.21). In other words the solution is approximately $\hat{p} \approx \gamma_c p_T \exp(i\omega t)$ in the liquid-like region of the cell and $\hat{p} \approx \gamma_h p_T \exp(i\omega t)$ in the gas-like region of the cell. Therefore the incremental pore pressure is in phase with the tidal loading over most of the convection cell.

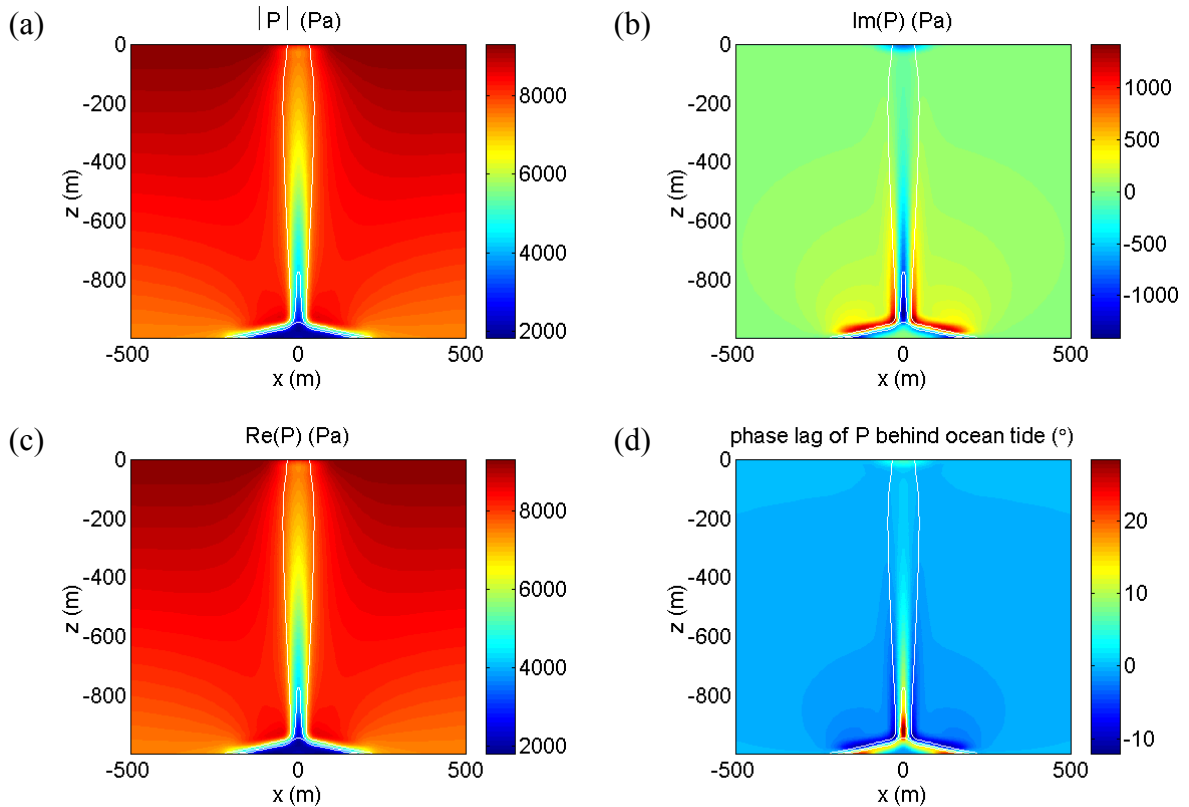


Figure 6.14: The complex incremental pore pressure amplitude $P(x,z)$ with $p_T = 10$ kPa, $d_c = 2.6$ m, $\gamma_c = 0.94$ and $\gamma_h = 0.14$. (a) The real part of the solution, representing the incremental pore pressure at high tide. (b) The imaginary part of the solution, representing the incremental pore pressure at rising half tide. (c) The magnitude of the incremental pore pressure. (d) The phase of the incremental pore pressure – expressed as a phase lag behind the ocean tide in degrees. In all figures, the isotherms at 300°C, 400°C and 500°C are drawn in white to illustrate the structure of the underlying convection cell (Figure 5.4).

Figure 6.15 shows the incremental pore pressure results with $k = 10^{-12}$ m², $\omega = 0.001$ s⁻¹. In this case, the larger value of the cold skindepth ($d_c = 26$ m) explains why the incremental pore pressure response of Figure 6.15 does not follow the boundaries in fluid properties (Figure 6.13) as closely as in Figure 6.14. The larger skindepth has led to a ‘smearing’ of the response across the boundary between the liquid-like and gas-like regions.

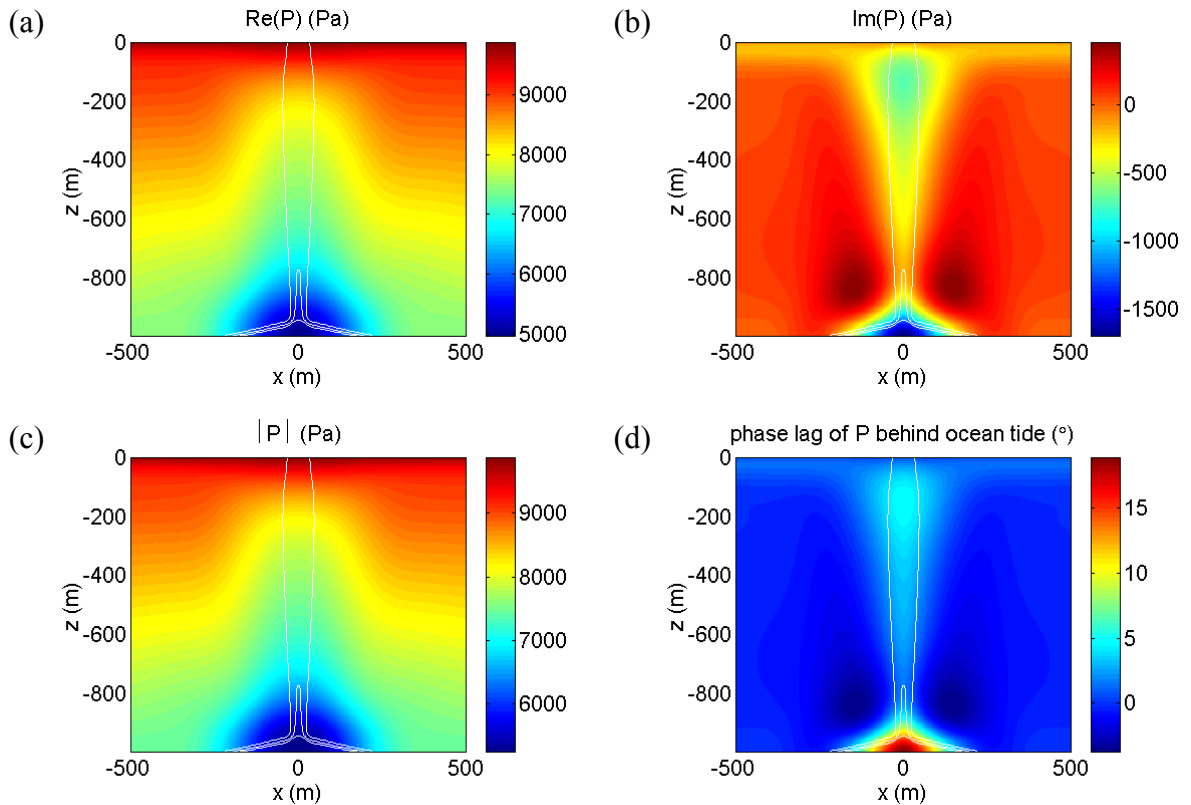


Figure 6.15: The complex incremental pore pressure amplitude $P(x,z)$ with $p_T = 10$ kPa, $d_c = 26$ m, $\gamma_c = 0.94$ and $\gamma_h = 0.14$. (a) The real part of the solution, representing the incremental pore pressure at high tide. (b) The imaginary part of the solution, representing the incremental pore pressure at falling half tide. (c) The magnitude of the incremental pore pressure. (d) The phase of the incremental pore pressure – expressed as a phase lag behind the ocean tide in degrees. In all figures, the isotherms at 300°C, 400°C and 500°C are drawn in white to illustrate the structure of the underlying convection cell (Figure 5.4).

Finally, Figure 6.16 shows the incremental pore pressure results with $k = 10^{-12}$ m² and $\omega = 0.000001$ s⁻¹. In this case, the cold skindepth ($d_c = 816$ m) is sufficiently large that incremental pore pressure response is dominated by the diffusive component over the entire convection cell.

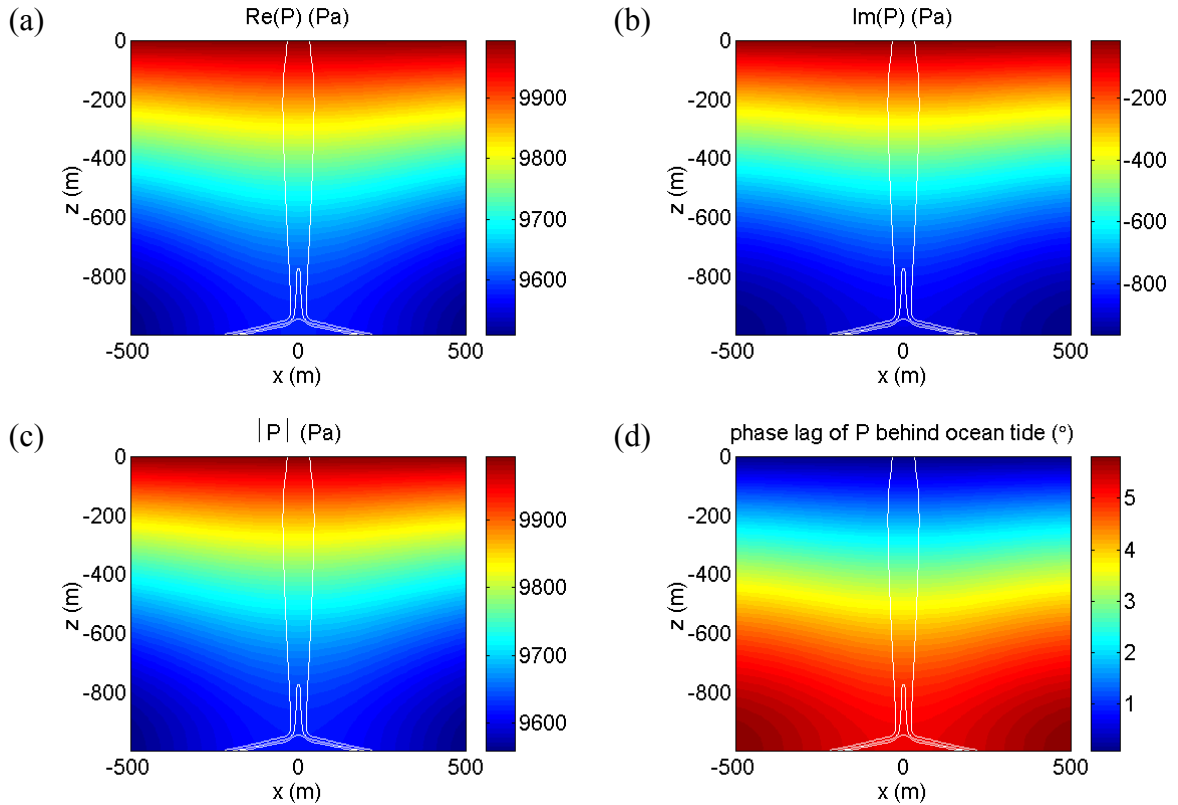


Figure 6.16: The complex incremental pore pressure amplitude $P(x,z)$ with $p_T = 10$ kPa, $d_c = 816$ m, $\gamma_c = 0.94$ and $\gamma_h = 0.14$. (a) The real part of the solution, representing the incremental pore pressure at high tide. (b) The imaginary part of the solution, representing the incremental pore pressure at rising half tide. (c) The magnitude of the incremental pore pressure. (d) The phase of the incremental pore pressure – expressed as a phase lag behind the ocean tide in degrees. In all figures, the isotherms at 300°C, 400°C and 500°C are drawn in white to illustrate the structure of the underlying convection cell (Figure 5.4).

In summary, Figures 6.14 – 6.16 illustrate the importance of the magnitude of the skindepth to the nature of the incremental pore pressure solution.

6.4 Conclusions

In this chapter, the application of the theory of poroelasticity to the tidal loading of subseafloor hydrothermal convection cells has been investigated.

The thermodynamic properties of water exert an important influence on the principal parameters of poroelasticity. At seafloor pressures, there is a marked difference between the properties of liquid-like water below $\sim 400^\circ\text{C}$ and gas-like water above $\sim 400^\circ\text{C}$. Consequently, it is predicted that the incremental pore pressure response to tidal loading in a hydrothermal convection cell varies spatially. The difference in response between the liquid-like and gas-like regions is greatest when the porosity is large.

The characteristic lengthscale of pore pressure diffusion induced by tidal loading is the skindepth (d). The skindepth depends on the permeability (k) which is very poorly constrained. For semi-diurnal loading, the skindepth can range from $d = 1 \text{ m}$ ($k = 10^{-17} \text{ m}^2$) to $d = 10,000 \text{ m}$ ($k = 10^{-10} \text{ m}^2$). The nature of the incremental pore pressure response depends on the magnitude of the skindepth compared with the lengthscales of the subseafloor convection cell. When the skindepth is much smaller than the lengthscales of the cell, the incremental pore pressure is given, over most of the cell, by the instantaneous response which is in phase with the ocean tide.

Van der Kamp & Gale (1983) derived an analytical solution for the incremental pore pressure in an infinite halfspace subject to tidal loading. In Section 6.3.1 their solution is extended in a number of ways. Firstly, it is used to provide expressions for the incremental velocity and temperature in an infinite halfspace. Secondly, an analogous incremental pore pressure solution is derived for the case of a permeable layer of finite vertical extent. This solution is also used to derive expressions for the incremental velocity and temperature in a finite permeable layer.

In the case of an infinite halfspace, it is shown that the tidally induced outflow at the seafloor lags the ocean tide by 135° for each tidal component. The magnitude of this tidally induced velocity is considered as a fraction of the steady effluent velocity. It is shown that the tidal modulations are greatest (as proportion of the steady effluent velocity) when the effluent is cool, the permeability is low and the frequency of the tidal loading is high. This last observation implies that the tidal modulations of effluent velocity measured at the seafloor are *high-pass filtered* relative to the ocean tide. In other words, semi-diurnal components should be amplified at the expense of diurnal components in comparison with the ocean tide. The incremental temperature in an infinite halfspace is calculated for the region just below the seafloor where the pressure and temperature are both linear functions of depth. It is

shown that the incremental temperature lags the incremental velocity by an angle which lies between 45° and 90° . The exact value of the phase lag depends on the permeability. For most plausible values of crustal permeability, the phase lag is almost exactly 90° . However, if the presence of cracks in the seafloor has led to a greatly enhanced seafloor permeability ($>10^{-10} \text{ m}^2$), the phase lag can take lower values in the range $[45^\circ, 90^\circ]$. For the infinite halfspace model, it follows that the incremental temperature lags the ocean tide by an angle in the range $[180^\circ, 225^\circ]$. The phase lag is almost exactly 225° for when the permeability is less than $\sim 10^{-10} \text{ m}^2$, but it approaches 180° as the permeability increases above $\sim 10^{-10} \text{ m}^2$.

In the case of a finite permeable layer of depth H , the behaviour of the analytical solutions is controlled by the parameter (H / d_{1d}) which expresses the thickness of the permeable layer in skindepths. The tidally induced effluent velocity at the seafloor is shown to lag the ocean tide by an angle in the range $[90^\circ, 135^\circ]$. The phase lag is almost exactly 135° for $(H / d_{1d}) > 2$, but it approaches 90° as $(H / d_{1d}) \rightarrow 0$. The amplitude of the tidally induced effluent velocity at the seafloor is compared with the result for an infinite halfspace. The amplitude of the outflow differs significantly from infinite halfspace result when $(H / d_{1d}) < 2$ and tends to zero as $(H / d_{1d}) \rightarrow 0$. The incremental temperature in a finite permeable layer lags the incremental velocity by an angle in the range $[45^\circ, 90^\circ]$ in exactly the same way as for an infinite halfspace. Consequently, the tidally induced temperature variations at the seafloor lag the ocean tide by an angle in the range $[135^\circ, 225^\circ]$ when the permeable layer is of finite thickness.

Consequently, the simple poroelastic results derived here are sufficient to explain effluent velocities which lag the ocean tide by an angle in the range $[90^\circ, 135^\circ]$, and effluent temperatures which lag the ocean tide by an angle in the range $[135^\circ, 225^\circ]$. This last range is consistent with the general (but by no means universal) observation that effluent temperatures tend to be low when the ocean tide is high – a situation that corresponds to a phase lag of 180° .

The theoretical predictions outlined above can now be compared with the phase-lags derived from real seafloor time-series (Table 4.13). It should be noted that these data refer to several different types of seafloor measurement which must be considered separately, and that the theory developed in this chapter does not apply to the majority of these signals.

The two hydrophone signals concern a physical process (episodic venting) which is not considered in any of the models developed in this dissertation. Consequently, no attempt is made to explain the phase-lags in these signals. Similarly, the measurements of ‘ambient bottom water temperature’ and ‘sub-bottom temperature’ are probably modulated by tidal streams and so the tidal loading mechanism explored above is not relevant. The estimated phase-lag for the ‘shrimp density’ time-series should be treated with *extreme* caution because the sampling interval of 6 h leads to unreliable estimates of the harmonic constants (Chapter 4). Consequently, there remain only three signals in Table 4.13 for which the phase-lags can be estimated with confidence and for which the theoretical model developed above is relevant - the two Medusa measurements of ‘effluent temperature’ and the thermistor measurements of ‘borehole temperature’. For these signals, the estimated phase-lags of the *M2A* component behind the local ocean tide are $\sim 180^\circ$, 225° and 140° (Table 4.13). These values all lie within the predicted range of $[135^\circ, 225^\circ]$ and are therefore consistent with the model.